Structural basis for coupling of the WASH subunit FAM21 with the endosomal SNX27-Retromer complex

Qian Guo[1,†], Kai-en Chen[1,†], Manuel Gimenez-Andres[2,†], Adam P. Jellett[2], Ya Gao[1], Boris Simonetti[2], Meihan Liu[1], Chris M. Danson[2], Kate J. Heesom[3], Peter J. Cullen[2,‡], Brett M. Collins[1,‡].

[1] The University of Queensland, Institute for Molecular Bioscience, St Lucia, Queensland, 4072, Australia.

[2] School of Biochemistry, Faculty of Life Sciences, Biomedical Sciences Building, University of Bristol, Bristol BS8 1TD, UK.

[3] Bristol Proteomics Facility, School of Biochemistry, Faculty of Life Sciences, Biomedical Sciences Building, University of Bristol, Bristol BS8 1TD, UK.

[†]Contributed equally

[‡]Corresponding author: pete.cullen@bristol.ac.uk; b.collins@imb.uq.edu.au

Running title: SNX27-Retromer interaction with WASH.

Key Words: Retromer, SNX27, endosome, WASH, AlphaFold, FAM21.

ABSTRACT

Endosomal membrane trafficking is mediated by specific protein coats and formation of actin-rich membrane domains. The Retromer complex coordinates with sorting nexin (SNX) cargo adaptors including SNX27, and the SNX27–Retromer assembly interacts with the WASH complex which nucleates actin filaments establishing the endosomal reycling domain. Crystal structures, modelling, biochemical and cellular validation reveal how the FAM21 subunit of WASH interacts with both Retromer and SNX27. FAM21 binds the FERM domain of SNX27 using acidic-Asp-Leu-Phe (aDLF) motifs similar to those found in the SNX1 and SNX2 subunits of the ESCPE-1 complex. Overlapping FAM21 repeats and a specific Pro-Leu containing motif bind three distinct sites on Retromer involving both the VPS35 and VPS29 subunits. Mutation of the major VPS35-binding site does not prevent cargo recycling, however it partially reduces endosomal WASH association indicating that a network of redundant interactions promote endosomal activity of the WASH complex. These studies establish the molecular basis for how SNX27–Retromer is coupled to the WASH complex via overlapping and multiplexed motif-based interactions required for the dynamic assembly of endosomal membrane recycling domains.

Significance Statement

Cell surface transmembrane proteins are regulated by a constant cycle of internalization and recycling from intracellular endosomal compartments. The Retromer protein complex and the sorting nexin adaptor protein play a critical role in the retrieval of hundreds of proteins responsible for ion transport, glucose metabolism, neurotransmission, and other cell functions. We have defined the mechanism by which both Retromer and SNX27 engage the actin-nucleating complex called WASH through multiple repeated sequences in the subunit FAM21. Dysfunction in WASH, Retromer and SNX27 are implicated in various disorders including Parkinson's disease, Alzheimer's disease, hereditary spastic paraplegia, and this work provides important insights into the assembly of these essential endosomal sorting machineries.

INTRODUCTION

Maintenance of appropriate levels of endosomal sorting of transmembrane 'cargo' proteins is essential for cellular function (1). Mammalian Retromer is an evolutionarily conserved protein complex composed of VPS35, VPS29, and VPS26 (two isoforms VPS26A and VPS26B) and is a central regulator of endosomal sorting across eukaryotes (2, 3). More specifically, it functions together with diverse accessory proteins and cargo adaptors to coordinate endosomal recruitment and sequence-specific cargo recognition with the assembly of endosomal sub-domains for the biogenesis of tubulovesicular transport carriers. Sorting nexin 27 (SNX27) is a Retromer cargo adaptor that binds to specific PSD95-DLG-ZO1 (PDZ) domain binding motif (PDZbm) containing cargo to promote their Retromer-dependent endosome-to-cell surface recycling (Lunn et al., 2007; Lauffer et al., 2010; Temkin et al., 2011; Steinberg et al., 2103; Gallon et al., 2014; Clairfeuille et al., 2016).

Both Retromer and SNX27 associate with the Wiskott-Aldrich Syndrome Protein and SCAR Homolog (WASH) complex, which by driving localised actin polymerisation plays an essential role in endosomal sorting and transport (4-10). The WASH complex is a pentamer of WASHC1, FAM21 (WASHC2), WASHC3 (coiled-coil domain-containing protein 53 (CCDC53)), WASHC4 (KIAA1033; WASH-interacting protein; SWIP) and WASHC5 (Strumpellin; KIAA0196) (5, 6, 11, 12). The WASHC1 subunit is a member of the Wiskott-Aldrich Syndrome Protein (WASP) family (11, 13), and the presence of a C-terminal verprolin homology sequence, connecting sequence, and acidic sequence (VCA) domain allows WASHC1 to activate the actin-related protein 2/3 (ARP2/3) complex to stimulate formation of branched F-actin networks (14). The ARP2/3 complex plays a number of roles in regulating endocytosis and subsequent endosomal sorting and transport processes (15-17).

During endosomal cargo sorting and transport, the WASH complex is essential for the fission of tubules during the biogenesis of transport carriers. Endosomal tubulation is exaggerated in cells lacking the WASH complex (6) and WASH depletion leads to the observation of long endosomal tubules aligned along microtubules (5). It is thought that WASH promotes the scission of cargo-containing tubules via generating F-actin-driven force at the endosomal membrane. Mutations in WASH complex subunits can result in neurological pathologies, such as hereditary spastic paraplegia, inherited intellectual disability, and late-onset Alzheimer's disease (12, 18-20).

Retromer regulates the recruitment of a population of the WASH complex to endosomal membranes (8, 9), while binding of WASHC4 to membrane phosphoinositide lipids can promote Retromer-independent mechanism of endosomal association (21). Native immunoprecipitations provided the initital evidence for the WASH complex interacting with Retromer, while yeast two-hybrid assays suggested direct associations between VPS35, FAM21 and WASHC1 (8). Suppression and knock-out of Retromer partly reduces WASH endosomal association (Harbour et al., 2010; McNally et al., 2017), while other members of the endosomal protein sorting system are unaffected, such as SNX1 and the RAB5 effector EEA1 (8). Structurally, FAM21 has a 200 amino acid "head" domain that interacts with the Strumpellin and WASHC1 proteins and is crucial for the formation and stabilisation of the WASH complex (9, 11). Following the head domain is a large (around 1100 amino acids) unstructured "tail" domain that contains 21 repeating motifs composed of Leu-Phe and

several acidic residues (Asp or Glu) dubbed LFa motifs (22). The enormous unstructured tail of FAM21 is important for membrane association (6), and it was shown that the LFa motifs can bind to the VPS35 subunit of Retromer with the C-terminal motifs most crucial for the interaction (22, 23). Overexpression of the FAM21 tail can displace the WASH complex on the endosome by competing for binding to VPS35 (9, 22, 23). Although the VPS35 subunit can associate with the FAM21 tail directly in yeast two-hybrid experiments and in isothermal titration calorimetry (ITC) assays (9, 22), binding is enhanced by other subunits when VPS35 is assembled into the functionally active Retromer complex (23). The interaction of Retromer with WASH via FAM21 is thought to link branched actin polymerisation to cargo protein sorting and trafficking activity, and the long unstructured nature of the FAM21 tail combined with the many LFa repeats likely promotes both avidity for Retromer and flexibility in the relative orientations for dynamic endosomal membrane sorting.

The SNX27 Retromer cargo adaptor was also reported to associate with the WASH complex by coimmunoprecipitation (4). Responsible for recycling over 400 specific transmembrane cargoes from endosomes to the plasma membrane (4, 24-27), SNX27 is a peripheral membrane protein containing, from N-termini to C-termini, PDZ, PX and FERM domains that mediate cargo selection, Retromer recruitment and protein-lipid interactions (26, 28, 29). Notably, SNX27 can bind via its FERM domain to acidic DLF (aDLF) motifs in the N-terminal disordered region of SNX1 and its homologue SNX2 within the BAR domain-containing ESCPE-1 complex (30, 31).

Here we show that the FAM21 subunit of WASH coordinates the interactions with both Retromer and SNX27 via very different mechanisms but incorporating distinct overlapping elements of the repeat sequences in its extended C-terminal domain. Crystal structures, modelling, biochemical and cellular experiments show that the multiple redundant acidic-Asp-Leu-Phe (aDLF) repeat sequences in FAM21 bind to a conserved basic pocket in the SNX27 FERM domains and are essentially identical to the aDLF sequences found in the endosomal proteins SNX1 and SNX2 (30). Overlapping repeated motifs in FAM21 with the consensus sequence [L/I]F[ED]$_{3\text{-}9}$[L/I]F bind two conserved sites towards the C-terminus of Retromer subunit VPS35. These lie opposite to the VSP29 binding site and adjacent to the dimerising surface required for assembling Retromer arches on the membrane. In addition, the last repeat of FAM21 contains a specific Asp-Pro-Leu sequence that binds a third site on VPS29 that is the same region bound by other interactors such as TBC1D5 and ANKRD27. Mutations in these regions perturb FAM21 interaction *in vitro* and in cells, however single mutations in VPS35 are not sufficient to block Retromer-mediated trafficking, consistent with a model whereby the WASH complex engages the endosome and associated proteins through multiple related but redundant motif-mediated interactions.

RESULTS

The FAM21 tail binds to both VPS35 and VPS29 through its repeat sequences

A primary characteristic of FAM21 is the long disordered tail enriched in acidic residues and containing 21 copies of a repeated [I/L]F sequence with C-terminal acidic residues (**Figures 1A and 1B**). This was previously termed the LFa motif and shown to bind directly to the Retromer subunit VPS35 with the final three repeats, 19-21, showing the strongest binding affinity (22). However, suggesting that VPS29 also plays a role in binding FAM21, we recently noted that binding of Retromer and GST-tagged FAM21 composed of repeats 19, 20 and 21 (GST-FAM21$_{R19-R21}$) was slightly reduced in the presence of a macrocyclic peptide that binds via a PL-containing sequence to a conserved site on the VPS29 subunit (32). To examine this, we first tested the binding between Retromer and peptides from human FAM21 repeat 19 (FAM21$_{R19}$), repeat 20 (FAM21$_{R20}$) and repeat 21 (FAM21$_{R21}$). Using ITC, we found FAM21$_{R21}$ alone was able to bind to Retromer, to the subcomplex composed of VPS29 and VPS35 residues 481 to 796 (VPS29–VPS35$_{481-796}$), as well as VPS29 alone (**Figure 1C; Table S1**). In contrast, FAM21$_{R19}$ and FAM21$_{R20}$ peptides showed a relatively weak Retromer interaction and no interaction at all with VPS29 (**Figure 1C)**. A stronger Retromer interaction was observed when we tested the GST-tagged construct combining repeats 19 and 20 (GST-FAM21$_{R19-R20}$), suggesting some additive effect of these two sequences (**Figure 1D)**. Notably the FAM21$_{R21}$ interaction with VPS29 on its own could be blocked by the addition of cyclic peptide RT-D1 (**Figure 1E**), indicating that FAM21$_{R21}$ likely binds to the same conserved VPS29 surface. Unlike other repeats FAM21 repeat 21 also contains a conserved DPL sequence next to the [I/L]Fa motif (**Figure 1B; Figure S1**) and it is this sequence that binds to VPS29 while other repeats bind to VPS35.

Structural basis for the interaction of FAM21 LFa repeats with VPS35

Our data suggests that FAM21 LFa repeats 19 and 20 interact with VPS35 while the divergent DPL-containing repeat 21 can bind VPS29. To understand the molecular basis of how the LFa repeating units bind to Retromer, we attempted to co-crystallize the VPS29–VPS35$_{481-796}$ subcomplex with FAM21$_{R19}$ and FAM21$_{R20}$ peptides. The structure of VPS29–VPS35$_{481-796}$ in complex with FAM21$_{R20}$ peptide was successfully solved at 3 Å resolution with two VPS29–VPS35$_{481-796}$ molecules in the asymmetric unit (**Figure 2A; Table S2**). Although the structure was solved at relatively low resolution, we could observe additional electron density on the surface of VPS35 representing the FAM21$_{R20}$ peptide (**Figure 2B**). The electron density for the FAM21$_{R20}$ peptide is located on a conserved positively charged groove of VPS35 between helices 23 and 25 surrounded by K552, K555, K556 and K559 (**Figures 2B and 2C**). To aid in assigning the FAM21$_{R20}$ residues into the structure as well as investigate the potential binding surface of repeat 19, we used AlphaFold2 modelling to predict complexes of different variations of FAM21 sequences bound to Retromer. These predictions consistently identified two separate binding sites on VPS35 for the FAM21$_{R19-R20}$ LFa repeats (**Figures 2D and 2E**). Inspecting these models closely, we found that repeats 19 and 20 are predicted to bind two distinct positively charged grooves at the C-terminal end of the VPS35 surface that we refer to as Site 1 and Site 2 respectively (**Figure 2E**). The X-ray crystallographic difference density for FAM21$_{R20}$ peptide aligns with Site 2 and matches well to the residues ^{1296}DDIF^{1299} of repeat 20 predicted in the model (**Figure 2F**). In particular

I1298 and F1299 are positioned to interact with K555, K556 and K559 of VPS35 (**Figure 2F**). A notable feature of the predicted structure is that in addtion to the ^{1296}DDIF^{1299} residues the repeated element engages VPS35 via an additional IF sequence interspersed with acidic residues ^{1290}IFDDDMDDIF^{1299} (**Figure 2F**). Similarly the predictions indicate that the second R19 sequence can bind to Site 1 with a similar dual [I/L]F motif with interspersed acidic residues ^{1262}LFDDNIDIF^{1270} recognising a second positively charged groove composed of K701, K705 and K749 (**Figure 2E**). With the combination of predictions and experimental structure we propose that VPS35 possesses two distinct binding sites for low affinity binding of the multiple LFa sequences in FAM21 (**Figure 1B**)(22). These structures indicate the definition of the LFa motif to ideally possess two [I/L]F sequences with an interveining stretch of Asp and Glu side chains [I/L]F[E/D]$_n$[I/L]F.

To further validate if both positively charged grooves of VPS35 are responsible for binding to FAM21 we performed co-immunoprecipitation with structurally targeted site-directed mutations of VPS35. Importantly, all mutants retained the ability to assemble into the Retromer heterotrimeric complex **(Figure 2G and 2H; Figure S2)**. Consistent with our structural data, binding to FAM21 was significantly affected by the multiple mutations around the repeat 20 binding grooves including K552, K555, K556 and K559 (**Figure 2G; Figure S2**). The strongest defect in FAM21 binding was observed with the triple mutant composed of K555, K556 and K559 (**Figures 2G and 2I; Figure 2G; Figure S2**), the residues known to form contact with the LFa motif in Site 2. In addition, mutations of other positively charged residues surrounding the core [I/L]F dipeptide including K515S also showed significant defects in binding. It is likely that these residues together form a large positively charged patch on VPS35 for the initial recognition of the acidic repeats of FAM21. A similar defect was also observed in the K701E mutant on the second positively charged groove of Site 1 (**Figure 2H**). Notably, we also observed a slight defect in FAM21 binding when we used the VPS35 D620N mutant, the mutation known to be involved in the Parkinson diseases (McGough et al., 2014; Zavodszky et al., 2014). The mutation is distal from the FAM21$_{R19}$ and FAM21$_{R20}$ binding sites but lies next to the VPS35-mediated Retromer dimerization interface as seen in the Retromer-SNX3 and Retromer-SNX-BAR tubular coat complexes (33) (**Figure 2J**). It is possible that the slight defect in FAM21 binding is indirectly caused by interference with Retromer dimerization.

Repeat 21 binds to VPS29 through a classic PL motif interaction

To better understand the association of FAM21 repeat 21 with Retromer we next crystallised the VPS29–VPS35$_{481-796}$ complex with the FAM21$_{R21}$ repeat and determined its crystal structure at a modest 3.4 Å resolution. The structure reveals two VPS29–VPS35$_{481-796}$ molecules in the asymmetric unit. Notably, the dimerization interface in this structure differ from that observed in the FAM21$_{R20}$ bound structure (**Figure 3A**). Depsite the low resolution, we could still observe additional electron density around the conserved hydrophobic pocket of VPS29 (**Figure 3A**). To unambiguously assign the key residues involve in the interaction, we then successfully solved the structure of the VPS29–FAM21$_{R21}$ peptide complex at 2.0 Å resolution (**Figure 3B**). The improved density allowed us to build the PL motif and upstream residues. According to the structure, we could unambiguously observe the density up to D1332, suggesting that the signature [I/L]Fa dipeptide located at position 1330 and 1331 was not involved in the binding (**Figure 3C**). In

direct contrast to the $FAM21_{R20}$ structure bound with VPS35, the $FAM21_{R21}$ reveals a typical PL motif binding mode to VPS29 that superposes well with the previous cyclic peptide structures (**Figure 3D**) and other previous complexes with RidL, TBC1D5, VARP and VPS35L (34-38).

Consistent with the two structures and our mutagenesis studies, AlphaFold2 predictions incorporating the FAM21 sequence with all three repeats 19-21 produce a model with the three repeats bound to the three distinct sites; R19 and R20 respectively binding Site 1 and Site 2 on VPS35 and R21 extending around to bind to the conserved VPS29 surface (**Figure 3E-3H**). Both $FAM21_{R20}$ and $FAM21_{R21}$ peptide observed in the crystal structures fit well to the various models generated by Alphafold2 (**Figure 3G**). It seems very likely other LFa repeats would have the capacity to interact with one or both sites in VPS35. Indeed further analysis using Alphafold2 supports the potential of other repeats to bind VPS35 with similar structures (**Figures 3H; Figure S3**), and we find that repeats 5 and 17 (although not repeat 15), show low affinity for Retromer (**Figure 3I**). Projecting these findings onto the VPS35-mediated Retromer dimer observed in cryotomography structures (33), we expect that the LFa repeats such as $FAM21_{R19,}$ $FAM21_{R20}$ and $FAM21_{R21}$ can potentially use at least two distinct binding modes to engage the membrane-associated Retromer complex. With Repeat 21 bound to VPS29 as the reference point, repeats 19 and 20 and other LFa repeats from FAM21 could physically associate with two adjacent Retromer complexes in *trans* (model 1) or with one copy of Retromer in *cis* (model 2) (**Figure 3J**).

Interaction of FAM21 aDLF motifs with the SNX27 FERM domain

In addition to Retromer, SNX27 has also been reported to bind FAM21 to enable proper cargo recycling (4, 39, 40). To confirm this interaction, we first examined the binding using co-immunoprecipitations with various truncation constructs of GFP-FAM21. Robust association was observed between SNX27 and C-terminal region of FAM21(1109-1341) and FAM21(1250-1341) (**Figure 4A**). A shorter construct of FAM21(1300-1341) however, which lacks all LFa repeats apart from repeat 21, was unable to bind. Using ITC, we found that full-length human SNX27 bound to GST-tagged $FAM21_{R19-21}$ with a K_d of ~6 μM (**Figure 4B; Table S3**). Similar binding affinity was also detected when the FERM domain ($SNX27_{FERM}$) was used instead of the full-length SNX27 (**Figure 4B**), suggesting that the interaction primarily occurs through the FERM domain. We also tested the binding of $SNX27_{FL}$ and $SNX27_{FERM}$ with peptides corresponding to individual repeats $FAM21_{R19}$, $FAM21_{R20}$ and $FAM21_{R21}$ (**Figure 4C and D**). The results further reinforced the co-immunoprecipitation experiments showing that both $FAM21_{R19}$ and $FAM21_{R20}$ peptides bind to SNX27 with a K_d of ~7 μM and ~20 μM respectively, while repeat 21 showed no detectable interaction.

We noted that LFa repeats 19 and 20 (but not repeat 21) also contain sequences that resemble the acidic DLF (aDLF) motifs found in SNX1 and SNX2 previously shown to bind to the FERM domain of SNX27 (30). Indeed, mutations in the $FAM21_{R20}$ peptide substituting the DIF sequence with DSS blocked interaction with $SXN27_{FL}$ completely (**Figure 4E**), indicating that the D[L/I]F motif within repeats 19 and 20 play a major role in binding to SNX27. Sequence analysis of all of the 21 repeats within FAM21, showed that 12 of them also included the same sequence pattern with poly-acidic resides in front of a conserved D[L/I]F motif (**Figure 4F**). We proposed that all of these repeats are potentially able to bind SNX27, and using $FAM21_{R5}$, $FAM21_{R8}$,

216 $FAM21_{R15}$ and $FAM21_{R17}$ peptides as examples we found all four showed micromolar binding affinity to
217 $hSXN27_{FERM}$ (**Figures 4G and 4H**). These ITC data together confirmed that the D[L/I]F motif is the main
218 region responsible for binding to the FERM domain of SNX27, while the poly-acidic residues prior to the
219 D[L/I]F motif play a critical role in facilitating the association.

220

221 ***FAM21 and SNX1/SNX2 share the same binding pocket in the SNX27 FERM domain.***

222 To confirm the molecular basis for how FAM21 binds to SNX27, we first applied Alphafold2 to predict models
223 of $SNX27_{FERM}$ in complex with the subset of FAM21 repeats containing the putative aDLF motifs. Consistent
224 with our expectation, all the FAM21 repeats were predicted to bind the same conserved pocket on the F3
225 module of the SNX27 FERM domain (**Figure S4**), also known to bind to the aDLF motifs from SNX1/SNX2
226 (30, 31). To validate the models we then co-crystallized $SNX27_{FERM}$ with several different FAM21 repeat
227 motifs and crystal structures were determined with $FAM21_{R15}$, $FAM21_{R19}$ and $FAM21_{R20}$. All three complexes
228 were solved in the same space group showing a single FERM domain in the asymmetric unit (**Figures 5A-5C;**
229 **Table S4**). The electron density of the aDLF motif region was clearly visible in the highly conserved positively
230 charged pocket of the SNX27 FERM domain (**Figures 5A-5C**). Superimposition of the three structures
231 revealed a high degree of similarity without any major differences (**Figures 5D and 5E**). Our structures also
232 superposed well to the SNX1 peptide bound complex published previously (30, 31) (**Figure 5F**).

233 To confirm the binding mode of SNX27 binding to FAM21 aDLF sequences we tested mutations in
234 key SNX27 residues. SNX27 R437D and R498D mutants failed to interact with $FAM21_{R19}$ peptide by ITC,
235 while K495D, K496D and K501D reduced binding compared to the wild-type SNX27 (**Figure 5G**). The same
236 pattern of binding was observed by co-immunoprecipitation of proteins from HEK293T cells (**Figure 5H**),
237 although interestingly the K495D, K496D and K501D mutants had a greater impact on the ESCPE-1 complex
238 interaction (represented by SNX6 in these experiments) than FAM21 and the WASH complex. This suggests
239 that R437D and R498D play a central role in forming contacts with both FAM21 and SNX1/SNX2-derived
240 aDLF peptides. In particular, R498 is likely to be responsible for electrostatic attraction with the poly-acidic
241 residues in front of the aDLF motifs. Indeed, comparative unbiased proteomic analysis comparing the
242 interactomes of wild-type SNX27 with the R498D mutant of SNX27 confirmed a significant reduction in
243 association of SNX27(R498D) with subunits of both the WASH and ESCPE-1 complexes (**Figure 5I; Figure**
244 **S5A; Table S2**).

245

246 ***VPS35 Sites 1 and 2 enhance WASH endosomal recruitment but are not required for endosome-to-plasma***
247 ***membrane recycling of Retromer-SNX27 cargo proteins.***

248 We and others previously established that mutations in SNX27 that block interactions with aDLF motifs
249 perturb endosomal retrieval and recycling of the SNX27-interacting cargo GLUT1 by the SNX27-Retromer-
250 ESCPE-1 pathway (30, 31). While this phenotype was ascribed to a defect in SNX1 and SNX2-containing
251 ESCPE-1 complex binding to SNX27 during the hand-over of retrieved cargo into newly forming tubular
252 transport carriers (Simonetti et al., 2022), our results here indicate that the SNX27(R498D) mutant not only
253 perturbs SNX1/SNX2 association but also binding to the WASH complex. Thus the defect in GLUT1 recycling

254 could be attributed to either or both of these interactions, and it is not possible to design highly specific SNX27
255 mutations to distinquish them. Similarly, mutation of VPS29 to perturb the binding of FAM21 R21 will also
256 preclude interactions with other essential proteins such as TBC1D5 and VARP (35, 41, 42). In addition, the
257 highly redundant nature of the multiple overlapping LFa/aDLF repeats in FAM21 preclude the design of single
258 point mutations in the FAM21 tail to test the role of specific sequences. Indeed, we found that although deletion
259 of repeats 19-21 (residues 1250-1341) in the tail could reduce both Retromer and SNX27 interactions (**Figure**
260 **4A**), individual point mutations in these repeats had no impact on binding (**Figure S5B**) demonstrating that no
261 single sequence is essential to mediate their binding.

262 To assess whether the interaction of the WASH complex with VPS35 was important for the endosomal
263 activity we first assessed the localisation of FAM21 in VPS35 knock-out HeLa cells followed by rescue
264 experiments with VPS35 mutations in both Site 1 and Site 2 (K555N/K556L/K559Q/K701E; NLQE
265 mutant)(see **Figure 2G and 2H**). VPS35 KO cells show a modest but significant reduction in the colocalisation
266 of FAM21 to SNX1-positive endosomal domains consistent with previous reports (Harbour et al., 2010;
267 McNally et al., 2017). Re-expression of VPS35-GFP WT can partially rescue this mislocalistion, however
268 VPS35(NLQE)-GFP is unable to restore FAM21 recruitment levels indicating the VPS35 interaction is
269 important for promoting WASH complex localisation. We next assessed the importance of VPS35 interactions
270 with FAM21 for receptor recycling. Rescue experiments were performed in both VPS35 knock-out HeLa cells
271 (**Figure 6B and C**), and in H4 cells (**Figure S5C**) with similar results. As expected, in VPS35 KO cells the
272 cell surface levels of SNX27-Retromer cargos including GLUT1 and Kidins220 were reduced. When GFP-
273 VPS35 was re-expressed the cell surface levels of these proteins recovered to normal levels. However, the
274 VPS35(NLQE)-GFP mutant was also able to rescue endosomal recycling of these cargos, suggesting that
275 reduced FAM21 binding to VPS35 on its own is not strictly required for the steady-state recycling of SNX27-
276 Retromer-dependent cargos. Previous studies directly targeting FAM21 have shown that its depletion or
277 knock-out leads to cargo sorting defects (39, 42). It is likely our data can be reconciled through the complex
278 multivalent nature of FAM21 association with Retromer, such that although the VPS35 interaction with
279 FAM21 reduces WASH interaction significantly (**Figure 2G and 2H**), and is required for a proportion of
280 WASH recruitment to endosomal retrieval domains, the other minor sites in VPS29 retain an ability to engage
281 FAM21 and may compensate for its loss. Further, FAM21 can interact with SNX27 and other endosomal
282 proteins such as the Commander complex (43, 44), and the population of WASH associated with endosomes
283 in the asbence of Retromer as seen here (**Figure 6A**) and in other studies (21) provide an added level of
284 potential compensation.
285

DISCUSSION

In this work we have defined the molecular mechanisms underpinning the direct interactions between Retromer, SNX27 and the WASH complex via the extended C-terminal domain of the FAM21 subunit. These interactions firmly establish the role of highly repetitive sequences in FAM21 for directly engaging both SNX27 and Retromer using distinct but overlapping sequence requirements. LFa repeats consist of two [L/I]F motifs interspersed by tracts of acidic side chains and mediate specific Retromer attachment through VPS35. Notably as this work was under review, a related study provided similar data relating to the Retromer interaction with FAM21 providing further support for the model (45). aDLF repeats consist of a D[L/I]F motif preceded by acidic residues, overlap with the LFa repeats and specifically interact with the FERM domain of SNX27 using a completely different mechanism. Combined with previous work (9, 22, 30), these studies lead to an evolving model for the assembly of the SNX27-Retromer-WASH endosomal recycling domain as one of extreme structural plasticity, sequence redundancy within FAM21, and molecular avidity between FAM21 and assembled oligomers of SNX27–Retromer on the endosomal membrane (**Figure 7**). This network of interactions will also incorporate other proteins known to interact with the FAM21 C-terminus, including the Commander assembly (43, 44, 46, 47), WDR91 (48), RME-8 (49), FKBP15 (9), as well as TBC1D23 which has also been shown to bind to FAM21's LFa repeats (50, 51).

Our data shows that the LFa repeat sequences in FAM21 interact with Retromer at two distinct sites, and this is important for promoting WASH association with Retromer recycling domains, but not strictly essential for recycling of SNX27-Retromer cargos. Opposite to the VPS29-binding surface the VPS35 subunit has two separate sites for binding the peptide motifs, centred on K552, K555, K556 and K559 near the centre of the VPS35 α-helical solenoid (Site 2) and around K701, K705 and K749 near the C-terminus (Site 1). The discovery of two distinct binding pockets was surprising, and points to the potential of both redundancy in motif interactions (each site appears to have similar potential for binding FAM21 repeats) and avidity for increased binding strength (covalently connected sequences in FAM21 binding to two sites simultaneously). The presence of two binding sites is somewhat reminiscent of the binding of bipartite nuclear localisation signals to major and minor surfaces of the α-helical solenoid of importins (52), or of the nuclear receptors with the highly redundant FG repeats in the nucleoporins (53) , although the mechanisms are completely different. Although we do not observe dramatic differences between the affinities of individual and multiple FAM21 repeats for Retromer by ITC, we propose that the combination of Retromer oligomerisation on the membrane (33, 54) with the multivalent nature of FAM21 interactions will promote a high level of specificity in WASH/Retromer engagement (55). Given the enormous extended structure of the FAM21 tail and the number of similar LFa motifs, FAM21 will readily interact with multiple Retromer complexes when organised into polymeric arches at the endosomal membrane. It is also worth noting that this will not lead to a specific stoichiometry for the Retromer/WASH interaction, but rather will promote formation of a heterogeneous and dynamic multivalent network.

In addition to the LFa sequences binding to VPS35, we identified a third binding site on the conserved surface of VPS29 for the final repeat of FAM21 which possesses a DPL sequence. This binds with modest affinity, and is likely inessential for direct Retromer-dependent endosomal recruitment of FAM21 (**Figure**

S5B) (Harbour et al., 2010; Harbour et al., 2012). We speculate however, that once the WASH complex has bound to Retromer and/or SNX27 that repeat 21 could then act to regulate the association of Retromer with other proteins that bind the same site such as TBC1D5 (35, 56, 57) or ANKRD27 (41) (**Figure 7**).

Retromer, SNX27 and WASH are intimately connected in the endosomal sorting and transport of numerous transmembrane proteins (58-60). The current model is that Retromer, along with SNX cargo adaptors such as SNX3 and SNX27, can establish endosomal retrieval sub-domains and membrane tubules enriched in cargo, and WASH is able to nucleate formation of branched actin filaments via Arp2/3 that enhance membrane tubulation and promote scission (Puthenveedu et al., 2010; Temkin et al., 2011). The capping-interacting motif (CPI) of FAM21 is responsible for recruiting uncapping dynactin mini-filaments, that then prime the WASH-induced actin branching (61). The first indications that Retromer and WASH cooperate in endosomal recycling demonstrated their colocalization and a direct interaction between the FAM21 C-terminal tail and the Retromer complex (6, 8, 9, 22). These studies also identified the 21 LFa repeats in the FAM21 tail and their importance for Retromer association (22). The C-terminal tail of FAM21 is sufficient for endosomal localisation (9), and Retromer is important for endosomal recruitment of WASH (8, 22, 23, 62, 63), although WASH can also be recruited through Retromer-independent mechanisms via FAM21 and WASHC4/SWIP subunits respectively (21). WASH depletion was also reported to result in exaggerated endosome-derived tubules (5, 6, 64), although this is not universally observed (39, 42, 65, 66).

Previous research established that the FERM domain of SNX27 associates with the aDLF motifs of SNX1 and SNX2 (30, 31), and our data now shows that FAM21 utilises an identical mechanism to engage with the SNX27 adaptor. As shown in **Figure 3F**, the sequence alignment with SNX1/SNX2 peptides shows the D[L/I]F triplet is the most important component for binding, and at least two acidic amino acids before this motif are also important for promoting electrostatic interactions with SNX27. SNX1 and SNX2 are SNX-BAR proteins and subunits of the ESCPE-1 complex along with SNX5 and SNX6 (30). Mutations targeting the aDLF motif in SNX1 or SNX2 that disrupted binding to SNX27 have highlighted the role of the SNX27-ESCPE-1 interaction in promoting the tubular-based endosomal exit and cell surface recycling of SNX27-Retromer cargo (Yong *et al*, 2021; Simonetti et al., 2022). The results here both extend these previous analyses and complicate their interpretation, as the SNX27(R498D) mutant disrupts not only ESCPE-1 binding but also FAM21 and WASH association. As it is impossible to design SNX27 mutations that only affect SNX1/SNX2 but not FAM21 binding (and *vice versa*), we currently cannot disentangle the individual roles of each interaction on SNX27-dependent trafficking, and effects could be due to either interaction or a combination of both. Overall, however, this further establishes that not only Retromer but also SNX27 serve as direct ligands for overlapping multivalent repeat sequences in the FAM21 tail.

Combined with previous studies, our work makes it clear that the formation of endosomal retrieval sub-domains involves a dynamic network of generally low affinity interactions between Retromer, SNX27, ESCPE-1 and the WASH complex (and not discussed here ANKRD50) (McGough et al., 2014; Kvainickas et al., 2017), that includes a series of polyvalent extended sequences in subunits of the ESCPE-1 and WASH complexes. Low affinity interactions ensure that coincidence sensing of cargo and accessory proteins is required to provide the avidity necessary for pathway progression. This builds into the network dynamic

instability where if the correct density of cargo and accessory proteins are not sufficient, one could consider these to be ‘checks and balances’, then sub-domain organisation and coat formation will not be stabilised and the pathway will not progress (67). A more detailed understanding of both the spatial and temporal regulation of the interactions within the SNX27-Retromer-WASH-ESCPE-1 pathway will be challenging due to the high degree of multivalent and low affinity interactions involved, but will be essential for a complete portrait of this endosomal retrieval and recycling pathway(s). Reconstituting this pathway *in vitro* on artificial membranes, as well as high-resolution live-cell imaging will be required to begin to answer these questions, but the work here provides a key mechanistic foundation for these studies.

MATERIAL AND METHODS:

Peptides

All synthetic peptides applied for ITC and X-ray crystallography were obtained from Genscript (USA and Singapore). The peptides were freshly lyophilized using a laboratory freeze dryer Martin Christ ALPHA 1-2 LDplus to avoid chemical residues. To obtain the peptide stock solutions with a final concentration of 30 mM and a neutral pH, the freeze-dried peptides were dissolved in 1M HEPES pH 7.5. For use in ITC and co-crystallisation screening experiments, the peptides were diluted in protein buffer: 20 mM Tris-HCl pH 7.5, 200 mM NaCl, 5% glycerol, 1 mM β-ME. The sequences of peptides utilised were: FAM21-R5$_{536-552}$ GLFSDEEDSEDLFSSQS, FAM21-R8$_{662-678}$ TSLFEEDEEDDLFAIAK, FAM21-R15$_{1124-1140}$ RGEADLFDSGDIFSTGT, FAM21-R17$_{1197-1213}$ NPFPLLEDEDDLFTDQK, FAM21-R19$_{1261-1274}$ NLFDDNIDIFADLT, FAM21-R20$_{1289-1302}$ SIFDDDMDDIFSSG, FAM21-R20$_{1289-1302(IF/SS)}$ SSSDDDMDDSSSSG, and FAM21-R21$_{1328-1341}$ SNIFDDPLNAFGGQ, and they were generated from human WASH complex subunit 2A (FAM21A), Q641Q2.

Molecular biology and cloning for recombinant protein production

For bacteria expression of human Retromer and Retromer subcomplex, DNA encoding full-length Vps26A, Vps29, Vps35 and Vps35$_{481-796}$ were cloned into either pET28a or pGEX4T2 vectors as described previously (32). For SNX27, the codon-optimized gene containing full-length human SNX27 was synthesized by GenScript® and cloned into pET28a vector as described previously (30). The FERM domain containing residues 271 to 528 was inserted into pMCSG7 vector containing a N-terminal His-TEV tag. Human FAM21 truncation constructs including FAM21$_{R19-21}$, FAM21$_{R19-20}$, and FAM21$_{R20-21}$, were coned into pGEX4T2 vector for expression as a thrombin-cleavable N-terminal GST fusion protein. All the mutant constructs were conducted using site-directed mutagenesis approach with custom designed primers. All DNA constructs were verified using DNA sequencing.

Protein expression and purification.

All the protein constructs in this study were expressed using BL21 (DE3) competent cells and induced by isopropyl-β-D-1-thiogalactoside (IPTG) approach. In all cases unless noted otherwise, the cells were cultivated in Ultra Yield™ flasks at 37˚C and 180 rpm until the cell density reached OD_{600} ~0.8. A final concentration of 0.8 mM IPTG was then added to the expression culture and further incubated for 16 h to 18 h at 20˚C. To achieve the optimal expression yield of hSNX27$_{FERM}$, a final concentration of 0.5 mM IPTG was added to the culture prior to the incubation at 20˚C. After expression, the cells were pelleted and harvested by 10 min of centrifugation using JLA 8.1 rotor at 6000 rpm, 4˚C. The cell pellets were either stored at -80˚C or immediately proceeded to purification.

Purification of Retromer was performed using the protocol described previously (32). In brief, the GST-tagged VPS29 co-expressed with VPS35 were mixed with the cell pellet of VPS26A. Cells were lysed through a Constant System TS-series high pressure cell disruptor in lysis buffer containing 50 mM Tris-HCl pH 7.5, 200 mM NaCl, 2 mM 2-Mercaptoethanol (β-ME), 1 mM benzamidine, 10 µg/mL deoxyribonuclease

410 I (DNase I). The soluble homogenate cleared by centrifugation was loaded onto Talon resin (Clonetech)
411 followed by glutathione Sepharose (GE Healthcare) to obtain the correct stoichiometry ratio of the Retromer
412 complex. For the VPS29 – $VPS35_{481-796}$ subcomplex and VPS29 alone, the purification was carried out using
413 glutathione Sepharose (GE Healthcare) directly. Removal of the fusion tag from Retromer, subcomplex and
414 VPS29 were performed using on-column cleavage with thrombin protease (Sigma-Aldrich) overnight at 4˚C.
415 The flow-through containing the fusion tag free protein was further purified using size-exclusion
416 chromatography (SEC) on a HiLoad® 16/600 Superdex 200 or Superdex 75 column equilibrated with buffer
417 containing 50 mM Tris-HCl pH 7.5, 200 mM NaCl, 2 mM β-ME. Purification of hSNX27 constructs were
418 carried our using protocol described previously (30). For the FAM21 constructs, the cell pellet of GST-tagged
419 FAM21 protein was resuspended in lysis buffer containing 20 mM Tris-HCl pH 7.5, 200 mM NaCl, 5%
420 glycerol, 2 mM β-ME, 1 mM benzamidine, and 10 μg/mL DNase I. Cells were lysed and centrifuged using the
421 same protocol as Retromer and SNX27. Supernatants of GST-tagged protein homogenates were loaded onto
422 glutathione Sepharose™ beads (GE healthcare). Prior to the elution, the protein-bound bead was washed with
423 100 ml of washing buffer containing 20 mM Tris-HCl pH 7.5, 200 mM NaCl, 2 mM β-ME. The elution buffer
424 then carried out using the same buffer as the washing buffer supplemented with freshly prepared 20 mM
425 reduced glutathione and the 1 X cOmplete™ EDTA-free protease inhibitor tablet. The protease inhibitor table
426 was added to protect the GST-tag from non-specific cleavage during purification. The SEC was performed as
427 the final purification step using HiLoad® 16/600 Superdex 200 or Superdex 75 (GE Healthcare) column pre-
428 equilibrated with buffer containing 50 mM Tris-HCl pH 7.5, 200 mM NaCl, 2 mM β-ME. Protein integrity
429 was validated using SDS-PAGE gel and concentration was measured using Nanodrop at $OD_{280.}$
430

431 **Isothermal titration calorimetry (ITC)**

432 All microcalorimetry experiments were carried out at 25˚C using a PEAQ ITC (Malvern, UK) in SEC buffer.
433 The interaction of Retromer and FAM21 peptides was carried out by titrating 400 - 600 μM of FAM21 peptides
434 into 15 - 20 μM of Retromer, VPS29 – $VPS35_{481-796}$ subcomplex or VPS29. The effect of the cyclic peptide
435 was performed by titrating 400 μM of FAM21 R21 peptides into 15 μM of VPS29 supplemented with 2 mM
436 RT-D1. In the native control, the cyclic peptide was substituted with equivalent percentage (v/v) of DMSO.
437 For the Retromer mutant experiment, 400 – 600 μM of GST-$FAM21_{R19-R20}$ or 600 μM of FAM21 R21 peptide
438 was titrated into either 15 - 20 μM of native Retromer or $Retromer_{K555N,\ K556L,\ K559Q}$ mutant. In the case of
439 SNX27 and FAM21 interaction, 300 μM of GST-$FAM21_{R19-21}$ was titrated into 12 μM of either $hSNX27_{FL}$ or
440 $hSNX27_{FERM}$. For the binding tests of FAM21 peptides to SNX27, 800 μM of the FAM21 peptides were titrated
441 into 20 μM $hSNX27_{FL}$ or $hSNX27_{FERM}$ proteins. Mutant binding experiment was performed by titrating 600
442 μM of $FAM21_{R19}$ peptide into 20 μM of either native or single point mutant form of $hSNX27_{FL}$.
443 All ITC experiments were performed with a single injection of 0.4 μL followed by a series of 12
444 injections of 3.2 μL each, spaced 180 seconds apart, and stirred at 850 rpm. By integrating the observed peaks
445 and subtracting the heats of dilution from the background, the heat exchange of interactions was calculated.
446 The thermodynamic parameters Kd, ΔH, ΔG, and −TΔS for all binding tests were obtained by fitting and
447 normalising data to a single-site binding model using the Malvern software package. The stoichiometry was

448 adjusted initially, and if the value was nearly 1, N was set to exactly 1.0 for computation. To ensure the data
449 were reproducible, each experiment was run at least twice.
450
451 **Crystallisation**
452 Crystallization screening was carried out using the hanging-drop vapour diffusion method at a temperature of
453 20˚C. To obtain the FAM21 R20 bound co-crystal structure, the purified VPS29 – $VPS35_{481-796}$ subcomplex
454 was mixed with 8 molar excesses of $FAM21_{R20}$ peptide solubilized in 1 M HEPES pH 7.5. Crystals were
455 observed in multiple different commercial screen conditions. Best diffracting quality crystals were obtained
456 using streak seeding approach in 24-well plate with a final protein concentration of 10 mg/ml under condition
457 comprising 0.1 M Sodium Citrate pH 4.2, 0.2 M NaCl 16% PEG1000. Rod shape crystals appeared after 1 day
458 and grew to optimal after 5 days incubation at 20˚C. In the case of FAM21 R21 bound co-crystal structure,
459 two different protein complexes were prepared. In the first case, the purified VPS29 – $VPS35_{481-796}$ subcomplex
460 was mixed with 5 molar excesses of $FAM21_{R21}$ peptide solubilized in 1 M HEPES pH 7.5 at a final
461 concentration of 12 mg/ml in condition containing 0.1 M MES pH 6.5, 0.1 M Magnesium Acetate, 10%
462 PEG10,000. Crystals appeared after 3 days of incubation at 20˚C. In the second case, the purified VPS29 was
463 mixed with 2 molar excesses of $FAM21_{R21}$ peptide at a final protein concentration of 15 mg/ml. The protein-
464 $FAM21_{R21}$ peptide complex crystals were obtained in condition composed of 0.2 M Magnesium Formate, 20%
465 PEG3350. Crystals appeared after 2 weeks of incubation at 20˚C.
466 To co-crystallize $hSNX27_{FERM}$ with FAM21 peptides, five-fold molar excesses of the $FAM21_{R15}$,
467 $FAM21_{R19}$ and $FAM21_{R20}$ peptides were added respectively to the purified $hSNX27_{FERM}$ to a final
468 concentration of 17 mg/ml. Additionally, 10 mM DTT was supplemented to protect free cysteines. For co-
469 crystallisation with peptide $FAM21_{R20}$, $hSNX27_{FERM}$ was buffer exchanged to buffer containing 20 mM Tris
470 pH 7.5, 100 mM NaCl, 5% glycerol and 1 mM β-ME. Initial needle-shaped crystals were observed in the
471 commercial screen condition ProPlex C11, which contains 0.1 M Sodium Cacodylate pH 6.5 and 25%
472 PEG4000. The best diffraction-quality crystals were produced in 24-well plate under conditions comprising
473 0.1 M Sodium Cacodylate pH 6.0 and 22.5% PEG4000; 0.1 M Sodium Cacodylate pH 6.5 and 25% PEG3350;
474 0.1 M Sodium Cacodylate pH 6.5 and 22.5% PEG4000 for $hSNX27_{FERM}$-$FAM21_{R15}$, $hSNX27_{FERM}$-$FAM21_{R19}$
475 and $hSNX27_{FERM}$-$FAM21_{R20}$ complexes respectively.
476
477 **Crystallographic data collection and structure determination**
478 The X-ray diffraction data were collected at 100 K on the MX2 beamlines at the Australian Synchrotron. All
479 the collected data were indexed and integrated by AutoXDS (68) and scaled using Aimless (69). Phase was
480 solved by molecular replacement using Phaser (70). Crystal structures of VPS29 – $VPS35_{481-796}$ – $FAM21_{R20}$
481 and VPS29 – $VPS35_{481-796}$ – $FAM21_{R21}$ were solved using Retromer subcomplex hVPS29 – $hVPS35_{483-780}$
482 (PDB ID: 2R17) as the initial model. In the case of VPS29 – $FAM21_{R21}$ complex, human VPS29 from Vps29
483 – RT-D2 complex structure (PDB ID: 6XS7) was used as the template. For $hSNX27_{FERM}$ – $FAM21_{R15}$,
484 $hSNX27_{FERM}$ – $FAM21_{R19}$ and $hSNX27_{FERM}$ – $FAM21_{R20}$ complexes, the $hSNX27_{FERM}$ model generated by
485 AlphaFold2 was used as the template. Structure refinement was performed using the PHENIX suite (71) with

iterative rebuilding of the model. The refined model was manually rebuilded using Coot guided by Fo - Fc difference maps. Data collection and refinement statistics are summarized in **Supplementary Table S3**. Sequence conservation was based on a T-Coffee multiple sequence alignment (72) and calculated using the ConSurf Server (73). Structural alignments and molecular figures were generated using PyMOL (Schrodinger, USA).

AlphaFold predictions of FAM21 peptides binding to hSNX27$_{FERM}$

We utilised the AlphaFold2 neural network (74) of the open-source ColabFold pipeline (75) to produce models of FAM21 peptides that associate with Retromer or the SNX27 FERM domain. In the case of Retromer – FAM21 complex, the sequences of VPS29, VPS35 and FAM21 repeats 1, 2, 3, 4, 15, 16, 19, 20 and 21 were applied. For SNX27 – FAM21 complex, 12 of the acidic DLF motifs of the FAM21 were modelled with the sequence of the human SNX27 FERM domain (residues 271 to 528, NP_112180). The default settings for ColabFold were used to construct multiple sequence alignments using MMseqs2 (76) and perform structural relaxing of the final peptide geometry with Amber (77), which resulted in the generation of three models for each peptide. Structural alignments and molecular figures were generated using PyMOL (Schrodinger, USA).

Antibodies

Antibodies used in this study were mouse monoclonal antibodies: GFP (clones 7.1 and 13.1; 11814460001; Roche, Germany) (1:2,000 for WB), DMT-1(sc-166884, Santa Cruz Biotechnology) (1:1,000 for WB), GADPH (97166, Cell Signaling Technologies) (1:1,000 for WB), ITGb1 (clone 18, BD610467, BD Biosciences) (1:1,000 for WB), N-Cadherin (13A9, Cell signaling technology) (1:1,000 for WB), SNX1 (clone 51/SNX1; 611482; BD, USA) (1:1,000 for WB, 1:200 for IF), SNX2 (clone 13/SNX2; 5345661; BD) (1:1,000 for WB), SNX6 (clone d-5, 365965; Santa Cruz Biotechnology, USA) (1:1,000 for WB), SNX27 (ab77799, Abcam, UK) (1:1,000 for WB), β-actin (A1978; Sigma-Aldrich, USA) (1:2,000 for WB), VPS29 (clone d-1, 398874; Santa Cruz Biotechnology) (1:200 for WB), WASHC5 (clone B-10, sc-377146) (1:1,000 for WB); rabbit monoclonal antibodies: CI-MPR (EPR6599; 124767; Abcam) (1:1,000 for WB), VPS35 (EPR11501(B); 157220; Abcam) (1:1,000 for WB), GLUT1 (ab115730, Abcam) (1:1,000 for WB); rabbit polyclonal antibodies: FAM21 (kind gift from Dan Billadeau) (1:1000 for WB, 1:400 for IF), KIDINS-220 (21856-1-AP, Proteintech) (1:1,000 for WB), LAT1 (5347S, Cell signaling technology) (1:1,000 for WB), GFP (GTX20290; GeneTex, USA) (WB 1:2,000), STEAP-3 (17186-1-AP, Proteintech) (1:1,000 for WB), VPS26A (23892; Abcam) (1:1,000 for WB), VPS35 (97545; Abcam) (1:1,000 for WB), VPS29 (98929; Abcam) (1:100 for WB), WASH1 (kind gift from Dan Billadeau) (1:1,000 for WB), WASHC4 (ABT69, Merck) (1:1,000 for WB); goat polyclonal antibody EEA1 (A121550, Antibodies.com) (1:200 for IF).

Cell culture and transfection

HeLa, HEK-293T and H4 cell lines were sourced from and authenticated by ATCC. Cells were grown under standard conditions in DMEM (Sigma-Aldrich) supplemented with 10% (v/v) FCS (Sigma-Aldrich) and 1% penicillin/streptomycin (Gibco, USA). For GFP-based immunoprecipitations, HEK293T cells were transfected

524 with GFP constructs using polyethylenimine (Sigma-Aldrich) and expression was allowed for 24-48 hours.
525 To produce stably expressing cells, HeLa and H4 cells were transduced with lentiviruses with the
526 constructs cloned in pXLG3.
527
528 **Biotinylation of cell surface proteins**
529 For surface biotinylation experiments, fresh Sulfo-NHS-SS Biotin (Thermo Fisher Scientific, #21217) was
530 dissolved in ice-cold PBS at pH 7.8 at a final concentration of 0.2 mg/ml. Cells were washed twice in ice-cold
531 PBS and placed on ice to slow down the endocytic pathway. Next, cells were incubated with the biotinylation
532 reagent for 30 minutes at 4˚C followed by incubation in TBS for 10 minutes to quench the unbound biotin.
533 The cells were then lysed in lysis buffer and equal amounts of their proteins were subjected to Streptavidin
534 beads-based affinity isolation (GE Healthcare, USA). After 30 minutes incubation at 4 degrees, the beads
535 where washed 3 times with PBS + 1% TX100 and 1.2M NaCl.
536
537 **Immunoprecipitation and quantitative western blot analysis**
538 For western blotting, cells were lysed in PBS with 1% (v/v) Triton X-100 and Pierce protease inhibitor cocktail
539 (Thermo Scientific). The protein concentration was determined with a BCA assay kit (Thermo Fisher Scientific,
540 USA), and equal amounts were resolved on NuPAGE 4% to 12% precast gels (Invitrogen, USA). Blotting was
541 performed onto polyvinylidene difluoride membranes (Immobilon-FL; EMD Millipore, USA) followed by
542 detection using the Odyssey infrared scanning system (LI-COR Biosciences, USA). For GFP-based
543 immunoprecipitations, HEK-293T cells were lysed 48 hours after transfection in immunoprecipitation buffer
544 (50 mM Tris-HCl, 0.5% (v/v) NP-40, and Roche protease inhibitor cocktail) and subjected to GFP trap
545 (ChromoTek, Germany). Immunoblotting was performed using standard procedures. Detection was performed
546 on an Odyssey infrared scanning system (LI-COR Biosciences) using fluorescently labeled secondary
547 antibodies.
548
549 **TMT-labelling, Nano LC-MS/MS and Proteomic data analysis**
550 Were performed as described previously (Simonetti et al., 2019; Healy et al., 2023).
551
552 **Immunofluorescence staining, image acquisition and analysis**
553 HeLa cells were seeded onto 13mm coverslips. One day after, cells were washed in PBS, fixed in 4% (v/v) for
554 20 minutes and washed again 3 times. Cells were permeabilized with 0.1% (v/v) Triton X-100, blocked in 1%
555 (w/v) BSA, incubated for 1h with primary antibodies followed by 30 minutes with secondary antibodies (Alexa
556 Fluor, Thermo Fisher Scientific) in 1% BSA. Coverslips were mounted onto glass microscope slides with
557 Fluoromount-G (Invitrogen). Microscopy images were collected at 37 °C with a Leica SP8 AOBS confocal
558 laser scanning microscope attached to a Leica DM I8 inverted epifluorescence microscope (Leica
559 Microsystems, Germany), with a 63x 1.4 NA oil immersion lens (506350, Leica Microsystems). Images were
560 acquired using LASX software (Leica microsystems). Colocalisation and fluorescence intensity analysis were

561 performed using Volocity 6.3 software (PerkinElmer) with automatic Costes background thresholding.
562 Immunofluorescence images were prepared in Volocity 6.3, ImageJ and Adobe Illustrator (Adobe).
563
564 **Statistical analysis of western blots and confocal microscopy**
565 Statistics for western blots and confocal microscopy images were calculated from a minimum of 3 independent
566 experimental repeats. Graphs were generated using GraphPad Prism 9 software (LaJolla, CA) plotting the the
567 mean value ± the standard error (SE) for each experimental condition. n represents the number of independent
568 experimental repeats. One-way ANOVA with Dunnett's multiple comparison test was used to assess
569 statistically significance. In all graphs, * = $p < 0.05$, ** = $p < 0.01$, *** = $p < 0.001$, **** = $p < 0.0001$.
570

ACKNOWLEDGEMENTS:

We acknowledge use of the University of Queensland Remote Operation Crystallization and X-ray (UQ ROCX) Facility and the assistance of G.King and K.A.Arachchige. X-ray data were collected on the MX1 and MX2 microfocus beamline at the Australian Synchrotron.

FUNDING:

B.M.C. is supported by an Investigator Grant Project Grant from the National Health and Medical Research Council (APP2016410 and APP1156493). We thank the Bristol Proteomics Facility at the University of Bristol. P.J.C. is supported by the Wellcome Trust (104568/Z/14/Z amd 220260/Z/20/Z), the MRC (MR/L007363/1 and MR/P018807/1), the Lister Institute of Preventive Medicine, and the Royal Society Noreen Murray Research Professorship (RSRP/R1/211004). A.P.J. was funded through an MRC PhD Studentship.

AUTHOR CONTRIBUTIONS:

Initial Concept: B.M.C., and P.J.C.

Concept development: all authors.

ITC and structural determination and analysis: Q.G. and K.C.

Biochemistry and cell biology analysis: M.G-A., A.P.J., B.S., and C.M.D.

Proteomic analysis: K.J.H.

Data analysis and Figure generation: Q.G., K.C., A.P.J., B.S., and M.G-A.

Funding acquisition: B.M.C., and P.J.C.

Supervision: B.M.C., and P.J.C.

Writing – 1st draft: Q.G. and K.C.

(Writing – review & editing: all authors)

CONFLICTS OF INTEREST:

The authors declare that they have no conflict of interest.

604 **FIGURES**

605 **Figure 1. Retromer VPS29 is responsible for binding to repeat 21 of FAM21.**

606 (**A**) Schematic diagram showing features of human FAM21, and highlighting the 21 LFa repeats in the
607 unstructured tail. (**B**) Sequences of the 21 LFa repeats within the FAM21 tail. Conserved [I/L]F residues are
608 shown in grey and acidic residues are in red. The PL residues of repeat 21 are highlighted in green. (**C**) ITC
609 thermograms showing the titration of Retromer, the VPS29–VPS35$_{481-796}$ subcomplex, and VPS29 alone with
610 FAM21$_{R19}$ (blue); FAM21$_{R20}$ (green); and FAM21$_{R21}$ (red) peptides. (**D**) Retromer shows binding to GST-
611 FAM21$_{R19-R20}$. (**E**) VPS29 and FAM21$_{R21}$ peptide interaction can be blocked by the addition of the PL-
612 sequence containing cyclic peptide RT-D1. All ITC graphs show the integrated (bottom) and normalized raw
613 data (top) fit with a single-site binding model.

614

615 **Figure 2. Structural basis for the interaction of LFa repeats with Retromer subunit VPS35.**

616 (**A**) Overall crystal structure of VPS29–VPS35$_{481-796}$ in complex with FAM21$_{R20}$ peptides showing both
617 complexes from the asymmetric unit. (**B**) VPS35 is highly conserved in the FAM21$_{R20}$ binding region. The
618 density corresponding to the FAM21$_{R20}$ peptide is shown in mesh using 2Fo–Fc map contoured at 1σ. Sequence
619 conservation of VPS35 was mapped with CONSURF (73). (**C**) The electrostatic surface map showing
620 FAM21$_{R20}$ binding location on VPS35. (**D**) Predicted alignment Error (PAE) plots of VPS29–VPS35$_{481-796}$–
621 FAM21$_{R19-R20}$ complexes generated by Alphafold2. (**E**) The predicted structure highlighting the per-residue
622 confidence score (pLDDT) between 0 to 100. Regions showing low pLDDT score (green and orange) are
623 likely to be unstructured. (**F**) Alignment of the Alphafold2 model of FAM21$_{R20}$ (cyan) and the crystal structure
624 (VPS35 in light purple, FAM21$_{R20}$ as light pink) highlighting the key interacting residues between FAM21$_{R20}$
625 and VPS35. The insert shows the refined electron density of the FAM21$_{R20}$ peptide observed in the crystal
626 structure. (**G**) Co-immunoprecipitation (co-IP) of C-terminal GFP-tagged VPS35mutants in the Site 2 binding
627 pocket in HEK293T cells. (**H**) Co-IP of C-terminal GFP-tagged VPS35 and mutants in the Site 1 binding
628 pocket. Quantitation of these Western blots is shown in **Figure S2.** (**I**) ITC analysis showing the binding of
629 GST-FAM21$_{R19-R20}$ with either native Retromer or VPS35 (K555N/K556L/K559Q) Site 2 mutant. All ITC
630 graphs show the integrated (bottom) and normalized raw data (top) fit with a single-site binding model. (**J**)
631 The locations of the Site 1 and Site 2 FAM21 repeat binding sites are shown in the context of the VPS35-
632 mediated Retromer dimer assembly derived from cryoelectron tomography (33). The location of the D620N
633 mutation linked to Parkinson's Disease is also indicated in cyan spheres.

634

635 **Figure 3. Structural basis for repeat 21 binding to VPS29 and model for Retromer engagement by**
636 **multiple FAM21 repeats.**

637 (**A**) Crystal structure of VPS29–VPS35$_{481-796}$ bound to the FAM21$_{R21}$ peptide. (**B**) Crystal structure of VPS29
638 in complex with FAM21$_{R21}$ peptide. (**C**) Enlarged view highlighting the refined density of FAM21$_{R21}$ peptide
639 peptide (2Fo–Fc map contoured at 1σ). (**D**) Structural alignment of the VPS29–FAM21$_{R21}$ peptide complex
640 with the VPS29–RT-D1 cyclic peptide complex (PDB ID 6XS5)(32) highlighting the PL motif binding region.
641 (**E**) Predicted alignment Error (PAE) plots showing the predicted structure of VPS29–VPS35$_{481-796}$–FAM21$_{R19-}$

642 $_{R21}$ complex generated by Alphafold2. (**F**) The predicted structure highlighting the per-residue confidence
643 score (pLDDT) between 0 to 100. Regions showing low pLDDT score (represents as green and orange) are
644 likely to be unstructured. (**G**) Superimposition of all the two crystal structures with the Alphafold2 model. (**H**)
645 Alphafold2 predictions of the complex of VPS29–VPS35 with either FAM21$_{R1-R2}$, FAM21$_{R3-R4}$ or FAM21$_{R15-}$
646 $_{R16}$ showing pairs of repeats predicted to bind to the same positively charged grooves as repeats FAM21$_{19-20}$.
647 (**I**) ITC thermogram showing the binding between Retromer with FAM21$_{R5}$ (red line), FAM21$_{R15}$ (blue line)
648 and FAM21$_{R17}$ (green) peptides. All ITC graphs show the integrated (right) and normalized raw data (left) fit
649 with a single-site binding model. (**J**) The locations of the FAM21 repeat 19 and 20 binding sites as well as the
650 VPS29-binding repeat 21 are shown in the context of the VPS35-mediated Retromer dimer assembly derived
651 from cryoelectron tomography (33) (PDB ID: 7BLN). The right panel shows two proposed binding models for
652 how FAM21 can bind to a Retromer dimer in *cis* or *trans*.
653
654 **Figure 4. FAM21 aDLF repeats also binds to the SNX27 FERM domain.**
655 (**A**) Co-IP of GFP-tagged FAM21 tail in HEK293T cells. Samples were analysed by quantitative fluorescence-
656 based western blotting. The band intensities of SNX27 and VPS35 were measured from n=3 independent
657 experiments using Odyssey software. The SNX27 and VPS35 band intensities, normalized to GFP
658 expression, are presented as the average fraction of the full length FAM21 tail. (**B**) ITC analysis
659 showing the binding between GST-FAM21$_{R19-21}$ and SNX27 (yellow line) and SNX27 FERM (blue line). (**C**)
660 Similar binding experiment showing the binding of FAM21 peptides FAM21$_{R19}$, FAM21$_{R20}$ and FAM21$_{R21}$
661 with either (**C**) SNX27 FL or (**D**) SNX27 FERM. (**E**) ITC thermogram comparing the binding between native
662 FAM21$_{R20}$ and ^{1298}IF^{1299} to SS mutant peptides with SNX27 FL. (**F**) List of FAM21 peptides containing the
663 same aDLF motif to those observed in SNX1 and SNX2. (**G**) ITC binding curves of the FAM21$_{R5}$, FAM21$_{R8}$
664 and FAM21$_{R17}$ peptides titrated into either (**G**) SNX27 FL or (**H**) SNX27 FERM. All ITC graphs show the
665 integrated (bottom) and normalized raw data (top) fit with a single-site binding model.
666
667 **Figure 5. Structural basis for SNX27 interaction with FAM21 aDLF repeats.**
668 (**A**) Crystal structures of the SNX27 FERM domain bound to aDLF repeats of FAM21. Top views show the
669 key region of SNX27 FERM involved in the binding to the FAM21 aDLF seqeunces (**A**) FAM21$_{R15}$, (**B**)
670 FAM21$_{R19}$ and (**C**) FAM21$_{R20}$. Middle panels show the electron density corresponding to a simulated-
671 annealing composite omit 2Fo–Fc map contoured at 1σ. Bottom panels show electrostatic surface potential of
672 SNX27 highlighting the positively charged pocket of SNX27 FERM. (**D**) Structural alignment showing the
673 high degree of similarity between all three complex structures. (**E**) Sequence conservation map highlighting
674 the conserved pocket of SNX27 FERM domain for binding to FAM21 aDLF motifs. (**F**) Structural alignment
675 of SNX27 bound to FAM21$_{R19}$ with the SNX27–SNX1$_{75-92}$ complex (PDB ID 7CT1; (31)) showing they bind
676 the same pocket. (**G**) ITC analysis showing the binding of the FAM21$_{R19}$ peptide with the native or mutant
677 forms of SNX27. The ITC graphs represent the integrated and normalized data fit with 1:1 ratio binding. (**H**)
678 Co-IP of GFP-SNX27 mutants and binding of WASH, Retromer and ESCPE-1 (represented by SNX6) proteins
679 assessed by Western blot. (**I**) Proteomic studies comparing the native SNX27 and mutated SNX27 R498D

680 binding capabilities with SNX27 interactors assessed by Co-IP (n = 6; derived from 2 biological repeats each
681 with 3 technical repeats). Mutation of the aDLF binding pocket causes disrupted interactions with most WASH
682 and ESCPE-1 subunits. The full list of detected proteins is provided in **Dataset S1**.
683
684 **Figure 6. VPS35 interaction with FAM21 contributes to its endosomal localization, but it is not strictly**
685 **required for SNX27–Retromer recycling.**
686 (**A**) VPS35 KO HeLa cells show a reduction in the colocalisation of FAM21 to SNX1-positive endosomal
687 domains. Re-expression of VPS35-GFP WT can partially rescue this mislocalistion, but the mutant
688 VPS35(NLQE)-GFP with both FAM21 sites mutated is unable to restore FAM21 recruitment levels. A total
689 of 90 cells were analyzed in each condition for colocalization between SNX1 and FAM21 across n=3
690 independent experiments. (**B**) VPS35 KO HeLa cells showed reduced cell surface levels of SNX27–Retromer
691 dependent cargos including GLUT1 and KIDINS220. VPS35 KO clonal line was stably transduced with
692 lentiviral particles containing VPS35-GFP WT or VPS35(NLQE)-GFP. Re-expression and rescue with both
693 constructs is able to rescue the cell surface levels of these cargos. This indicates that full binding of FAM21
694 to VPS35 is not strictly required for SNX27–Retromer mediated endosomal recycling. (**C**) Quantitation of
695 Western blots is shown. Similar results were obtained in H4 cell lines as shown in **Figure S5C**. Statistics for
696 western blots and confocal microscopy images were calculated from a minimum of 3 independent experimental
697 repeats Graphs were plotted representing the mean value ± the standard error (SE) for each experimental
698 condition. s. In all graphs, * = $p < 0.05$, ** = $p < 0.01$, *** = $p < 0.001$, **** = $p < 0.0001$.
699
700
701 **Figure 7. Summary and proposed model for the cooperative recruitment of FAM21 by Retromer,**
702 **SNX27 and other endosomal proteins.**
703 The WASH subunit FAM21 has 21 LFa repeated elements in its extended tail that are rich in acidic, isoleucine
704 and phenylalanine residues. LFa sequences possess two [L/I]F motifs interspersed by an acidic stretch
705 ([L/I]F[D/E]$_{3\text{-}9}$[L/I]F). These bind two conserved sites towards the C-terminus of the VPS35 subunit of
706 Retromer. The last repeated element of FAM21 has a specific PL dipeptide sequence that promotes interaction
707 with Retromer subunit VPS29. This would be mutually exclusive of binding to other VPS29 interactors such
708 as TBC1D5, ANKRD27, VPS35L and bacterial effector RidL. aDLF sequences are a subset of the LFa repeats
709 with an acidic stretch prior to a D[L/I]F motif that associate with a conserved pocket in the SNX27 FERM
710 domain, and are also found in the SNX1 and SNX2 proteins of the ESCPE-1 complex.
711
712
713

SUPPLEMENTARY FIGURES AND DATA

Figure S1. Sequence alignment of FAM21/WASHC2 repeats 19, 20 and 21.

Repeats 19-21 of FAM21 are aligned from various species. Conserved [I/L]F dipeptide motifs are indicated by yellow arrows while the specific PL motif in repeat 21 is indivated by green ovals. h, homo sapiens; m, Mus musculus; r, Rattus norvegicus; b, Bos taurus; d, Drosophila melanogaster; zf, Danio rerio.

Figure S2. Quantitation of the Western blots shown in Figure 2G and 2H.

Band intensities from **Figure 2G and 2H** were quantified using Odyssey software and normalized to GFP expression. 1-way ANOVA with Dunnett's multiple comparisons test. Error bars represent the standard error. *P < 0.05, **P < 0.01, ***P < 0.001, ****P < 0.0001.

Figure S3. Alphafold models of VPS35–VPS29 in complex with different FAM21 LFa repeats.

(**A**) Predicted alignment Error (PAE) plots for the AlphaFold2-predicted structures of the human (**A**) VPS35–VPS29–FAM21$_{R1-R2}$ complex, (**B**) VPS35–VPS29–FAM21$_{R3-R4}$ complex, (**C**) VPS35–VPS29–FAM21$_{R15-R16}$ complex. On the right the predicted structures are shown coloured according to the per-residue confidence score (pLDDT) between 0 to 100. Regions showing a low pLDDT score (green and orange) are likely to be unstructured.

Figure S4. Alphafold models of SNX27 FERM domain in complex with various FAM21 aDLF sequences.

(**A**) Overlay of all AlphaFold2 predicted structures shown as Cα backbone ribbon. The sequences of the aDLF repeats are shown in **Figure 4F.** (**B**) The predicted complex of SNX27$_{FERM}$ bound to FAM21 aDLF sequence from repeat 1. SNX27 is shown in cartoon representation coloured according to pLDDT score. The FAM21$_{R1}$ peptide is shown in green sticks. (**C**) Predicted alignment Error (PAE) plots showing the predicted structure of human SNX27$_{FERM}$–FAM21 aDLF complexes. The top ranked prediction is shown in close up in the left hand panels.

Figure S5. Interactions of SNX27 and FAM21 mutants and VPS35 rescue experiments in H4 cells.

(**A**) Co-IP in HEKs of GFP-SNX27 wild-type and R498D mutant and binding of WASH, Retromer (indicated by subunit VPS26A) and model cargo KIDINS220 assessed by Western blot. (**B**) Co-IP of GFP-FAM21 and mutants shows that specific mutations in repeats 19-21 do not prevent binding to Retromer or SNX27 in cells. KK is the combination of D1268K and D1297K mutants. (**C**) VPS35 KO H4 cells showed reduced cell surface levels of SNX27–Retromer dependent cargos including CTR1, GLUT1 and KIDINS220. Re-expression and rescue with both GFP-VPS35 wild-type protein and VPS35(NLQE)-GFP is able to rescue the cell surface levels of these cargos. This indicates that Site 2 in VPS35 is not strictly required for SNX27–Retromer mediated endosomal recycling. Band intensities for all blots were quantified using Odyssey software and normalized to GFP expression. 1-way ANOVA with Dunnett's multiple comparisons test. Error bars represent the mean, s.d. *P < 0.05, **P < 0.01, ***P < 0.001, ****P < 0.0001.

752 **Dataset S1. Proteomic interactions of GFP-SNX27(R498D) mutant versus GFP-SNX27 wild type.**

753

754 **REFERENCES:**

755

756 1. P. J. Cullen, F. Steinberg, To degrade or not to degrade: mechanisms and significance of endocytic
757 recycling. *Nat Rev Mol Cell Biol* **19**, 679-696 (2018).

758 2. C. Burd, P. J. Cullen, Retromer: a master conductor of endosome sorting. *Cold Spring Harb Perspect*
759 *Biol* **6** (2014).

760 3. K. E. Chen, M. D. Healy, B. M. Collins, Towards a molecular understanding of endosomal trafficking
761 by Retromer and Retriever. *Traffic* **20**, 465-478 (2019).

762 4. F. Steinberg *et al.*, A global analysis of SNX27-retromer assembly and cargo specificity reveals a
763 function in glucose and metal ion transport. *Nat Cell Biol* **15**, 461-471 (2013).

764 5. E. Derivery *et al.*, The Arp2/3 activator WASH controls the fission of endosomes through a large
765 multiprotein complex. *Dev Cell* **17**, 712-723 (2009).

766 6. T. S. Gomez, D. D. Billadeau, A FAM21-containing WASH complex regulates retromer-dependent
767 sorting. *Dev Cell* **17**, 699-711 (2009).

768 7. T. S. Gomez, J. A. Gorman, A. A. de Narvajas, A. O. Koenig, D. D. Billadeau, Trafficking defects in
769 WASH-knockout fibroblasts originate from collapsed endosomal and lysosomal networks. *Mol Biol*
770 *Cell* **23**, 3215-3228 (2012).

771 8. M. E. Harbour *et al.*, The cargo-selective retromer complex is a recruiting hub for protein complexes
772 that regulate endosomal tubule dynamics. *J Cell Sci* **123**, 3703-3717 (2010).

773 9. M. E. Harbour, S. Y. Breusegem, M. N. Seaman, Recruitment of the endosomal WASH complex is
774 mediated by the extended 'tail' of Fam21 binding to the retromer protein Vps35. *Biochem J* **442**, 209-
775 220 (2012).

776 10. P. Temkin *et al.*, SNX27 mediates retromer tubule entry and endosome-to-plasma membrane
777 trafficking of signalling receptors. *Nat Cell Biol* **13**, 715-721 (2011).

778 11. D. Jia *et al.*, WASH and WAVE actin regulators of the Wiskott-Aldrich syndrome protein (WASP)
779 family are controlled by analogous structurally related complexes. *Proc Natl Acad Sci U S A* **107**,
780 10442-10447 (2010).

781 12. P. N. Valdmanis *et al.*, Mutations in the KIAA0196 gene at the SPG8 locus cause hereditary spastic
782 paraplegia. *Am J Hum Genet* **80**, 152-161 (2007).

783 13. S. B. Padrick, M. K. Rosen, Physical mechanisms of signal integration by WASP family proteins.
784 *Annu Rev Biochem* **79**, 707-735 (2010).

785 14. L. E. Burianek, S. H. Soderling, Under lock and key: spatiotemporal regulation of WASP family
786 proteins coordinates separate dynamic cellular processes. *Semin Cell Dev Biol* **24**, 258-266 (2013).

787 15. S. N. Duleh, M. D. Welch, WASH and the Arp2/3 complex regulate endosome shape and trafficking.
788 *Cytoskeleton (Hoboken)* **67**, 193-206 (2010).

789 16. M. Park, H. J. Kim, B. Lim, A. Wylegala, M. Toborek, Methamphetamine-induced occludin
790 endocytosis is mediated by the Arp2/3 complex-regulated actin rearrangement. *J Biol Chem* **288**,
791 33324-33334 (2013).

792 17. R. Chakrabarti, M. Lee, H. N. Higgs, Multiple roles for actin in secretory and endocytic pathways.
793 *Curr Biol* **31**, R603-R618 (2021).

794 18. S. T. de Bot *et al.*, Pure adult-onset spastic paraplegia caused by a novel mutation in the KIAA0196
795 (SPG8) gene. *J Neurol* **260**, 1765-1769 (2013).

796 19. F. Ropers *et al.*, Identification of a novel candidate gene for non-syndromic autosomal recessive
797 intellectual disability: the WASH complex member SWIP. *Hum Mol Genet* **20**, 2585-2590 (2011).

798 20. B. N. Vardarajan *et al.*, Identification of Alzheimer disease-associated variants in genes that regulate
799 retromer function. *Neurobiol Aging* **33**, 2231 e2215-2231 e2230 (2012).

800 21. V. Dostál, T. Humhalová, P. Beránková, O. Pácalt, L. Libusová, SWIP mediates retromer-independent
801 membrane recruitment of the WASH complex. *bioRxiv* 10.1101/2022.08.16.504073,
802 2022.2008.2016.504073 (2022).

803 22. D. Jia, T. S. Gomez, D. D. Billadeau, M. K. Rosen, Multiple repeat elements within the FAM21 tail
804 link the WASH actin regulatory complex to the retromer. *Mol Biol Cell* **23**, 2352-2361 (2012).

805 23. E. Helfer *et al.*, Endosomal recruitment of the WASH complex: active sequences and mutations
806 impairing interaction with the retromer. *Biol Cell* **105**, 191-207 (2013).

807 24. B. Balana *et al.*, Mechanism underlying selective regulation of G protein-gated inwardly rectifying
808 potassium channels by the psychostimulant-sensitive sorting nexin 27. *Proc Natl Acad Sci U S A* **108**,
809 5831-5836 (2011).

810 25. R. Ghai *et al.*, Phox homology band 4.1/ezrin/radixin/moesin-like proteins function as molecular
811 scaffolds that interact with cargo receptors and Ras GTPases. *Proc Natl Acad Sci U S A* **108**, 7763-
812 7768 (2011).

813 26. R. Ghai *et al.*, Phosphoinositide binding by the SNX27 FERM domain regulates its localization at the
814 immune synapse of activated T-cells. *J Cell Sci* **128**, 553-565 (2015).

815 27. M. Gallon *et al.*, A unique PDZ domain and arrestin-like fold interaction reveals mechanistic details
816 of endocytic recycling by SNX27-retromer. *Proc Natl Acad Sci U S A* **111**, E3604-3613 (2014).

817 28. T. Clairfeuille *et al.*, A molecular code for endosomal recycling of phosphorylated cargos by the
818 SNX27-retromer complex. *Nat Struct Mol Biol* **23**, 921-932 (2016).

819 29. Y. Li, S. Liao, F. Li, Z. Zhu, Crystal Structure of the PX Domain of SNX27. *Biochemistry (Mosc)* **84**,
820 147-152 (2019).

821 30. B. Simonetti *et al.*, SNX27-Retromer directly binds ESCPE-1 to transfer cargo proteins during
822 endosomal recycling. *PLoS Biol* **20**, e3001601 (2022).

823 31. X. Yong *et al.*, SNX27-FERM-SNX1 complex structure rationalizes divergent trafficking pathways
824 by SNX17 and SNX27. *Proc Natl Acad Sci U S A* **118** (2021).

825 32. K. E. Chen *et al.*, De novo macrocyclic peptides for inhibiting, stabilizing, and probing the function
826 of the retromer endosomal trafficking complex. *Sci Adv* **7**, eabg4007 (2021).

827 33. N. Leneva, O. Kovtun, D. R. Morado, J. A. G. Briggs, D. J. Owen, Architecture and mechanism of
828 metazoan retromer:SNX3 tubular coat assembly. *Sci Adv* **7** (2021).

829 34. M. Romano-Moreno *et al.*, Molecular mechanism for the subversion of the retromer coat by the
830 Legionella effector RidL. *Proc Natl Acad Sci U S A* **114**, E11151-E11160 (2017).

831 35. D. Jia *et al.*, Structural and mechanistic insights into regulation of the retromer coat by TBC1d5. *Nat*
832 *Commun* **7**, 13305 (2016).

833 36. D. J. Boesch *et al.*, Structural Organization of the Retriever-CCC Endosomal Recycling Complex.
834 *bioRxiv* 10.1101/2023.06.06.543888, 2023.2006.2006.543888 (2023).

835 37. M. D. Healy *et al.*, Structure of the endosomal Commander complex linked to Ritscher-Schinzel
836 syndrome. *Cell* **186**, 2219-2237 e2229 (2023).

837 38. S. Laulumaa, E.-P. Kumpula, J. T. Huiskonen, M. Varjosalo, Structure and Interactions of the
838 Endogenous Human Commander Complex. *bioRxiv* 10.1101/2023.04.03.535349,
839 2023.2004.2003.535349 (2023).

840 39. S. Lee, J. Chang, C. Blackstone, FAM21 directs SNX27-retromer cargoes to the plasma membrane by
841 preventing transport to the Golgi apparatus. *Nat Commun* **7**, 10939 (2016).

842 40. A. Kvainickas *et al.*, Retromer- and WASH-dependent sorting of nutrient transporters requires a
843 multivalent interaction network with ANKRD50. *J Cell Sci* **130**, 382-395 (2017).

844 41. H. Crawley-Snowdon *et al.*, Mechanism and evolution of the Zn-fingernail required for interaction of
845 VARP with VPS29. *Nat Commun* **11**, 5031 (2020).

846 42. I. J. McGough *et al.*, Identification of molecular heterogeneity in SNX27-retromer-mediated
847 endosome-to-plasma-membrane recycling. *J Cell Sci* **127**, 4940-4953 (2014).

848 43. K. E. McNally *et al.*, Retriever is a multiprotein complex for retromer-independent endosomal cargo
849 recycling. *Nat Cell Biol* **19**, 1214-1225 (2017).

850 44. A. Singla *et al.*, Endosomal PI(3)P regulation by the COMMD/CCDC22/CCDC93 (CCC) complex
851 controls membrane protein recycling. *Nat Commun* **10**, 4271 (2019).

852 45. M. Romano-Moreno, E. N. Astorga-Simón, A. L. Rojas, A. Hierro, Retromer-mediated recruitment of
853 the WASH complex involves discrete interactions between VPS35, VPS29 and Fam21. *bioRxiv*
854 10.1101/2024.01.22.576619, 2024.2001.2022.576619 (2024).

855 46. P. Bartuzi *et al.*, CCC- and WASH-mediated endosomal sorting of LDLR is required for normal
856 clearance of circulating LDL. *Nat Commun* **7**, 10961 (2016).

857 47. C. A. Phillips-Krawczak *et al.*, COMMD1 is linked to the WASH complex and regulates endosomal
858 trafficking of the copper transporter ATP7A. *Mol Biol Cell* **26**, 91-103 (2015).

859 48. N. Liu, K. Liu, C. Yang, WDR91 specifies the endosomal retrieval subdomain for retromer-dependent
860 recycling. *J Cell Biol* **221** (2022).

861 49. C. L. Freeman, G. Hesketh, M. N. Seaman, RME-8 coordinates the activity of the WASH complex
862 with the function of the retromer SNX dimer to control endosomal tubulation. *J Cell Sci* **127**, 2053-
863 2070 (2014).

864 50. W. Huang *et al.*, Structural and functional studies of TBC1D23 C-terminal domain provide a link
865 between endosomal trafficking and PCH. *Proc Natl Acad Sci U S A* **116**, 22598-22608 (2019).

866 51. J. J. H. Shin, A. K. Gillingham, F. Begum, J. Chadwick, S. Munro, TBC1D23 is a bridging factor for
867 endosomal vesicle capture by golgins at the trans-Golgi. *Nat Cell Biol* **19**, 1424-1432 (2017).

868 52. M. Christie *et al.*, Structural Biology and Regulation of Protein Import into the Nucleus. *J Mol Biol*
869 **428**, 2060-2090 (2016).

870 53. R. H. Kehlenbach, P. Neumann, R. Ficner, A. Dickmanns, Interaction of nucleoporins with nuclear
871 transport receptors: a structural perspective. *Biol Chem* **404**, 791-805 (2023).

872 54. O. Kovtun *et al.*, Structure of the membrane-assembled retromer coat determined by cryo-electron
873 tomography. *Nature* **561**, 561-564 (2018).

874 55. K. Teilum, J. G. Olsen, B. B. Kragelund, On the specificity of protein-protein interactions in the
875 context of disorder. *Biochem J* **478**, 2035-2050 (2021).

876 56. M. N. Seaman, M. E. Harbour, D. Tattersall, E. Read, N. Bright, Membrane recruitment of the cargo-
877 selective retromer subcomplex is catalysed by the small GTPase Rab7 and inhibited by the Rab-GAP
878 TBC1D5. *J Cell Sci* **122**, 2371-2382 (2009).

879 57. M. N. J. Seaman, A. S. Mukadam, S. Y. Breusegem, Inhibition of TBC1D5 activates Rab7a and can
880 enhance the function of the retromer cargo-selective complex. *J Cell Sci* **131** (2018).

881 58. A. I. Fokin, A. M. Gautreau, Assembly and Activity of the WASH Molecular Machine: Distinctive
882 Features at the Crossroads of the Actin and Microtubule Cytoskeletons. *Front Cell Dev Biol* **9**, 658865
883 (2021).

884 59. B. Simonetti, P. J. Cullen, Actin-dependent endosomal receptor recycling. *Curr Opin Cell Biol* **56**, 22-
885 33 (2019).

886 60. M. N. Seaman, A. Gautreau, D. D. Billadeau, Retromer-mediated endosomal protein sorting: all
887 WASHed up! *Trends Cell Biol* **23**, 522-528 (2013).

888 61. A. I. Fokin *et al.*, The Arp1/11 minifilament of dynactin primes the endosomal Arp2/3 complex. *Sci*
889 *Adv* **7** (2021).

890 62. E. Zavodszky *et al.*, Mutation in VPS35 associated with Parkinson's disease impairs WASH complex
891 association and inhibits autophagy. *Nat Commun* **5**, 3828 (2014).

892 63. I. J. McGough *et al.*, Retromer binding to FAM21 and the WASH complex is perturbed by the
893 Parkinson disease-linked VPS35(D620N) mutation. *Curr Biol* **24**, 1670-1676 (2014).

894 64. P. V. Ryder *et al.*, The WASH complex, an endosomal Arp2/3 activator, interacts with the Hermansky-
895 Pudlak syndrome complex BLOC-1 and its cargo phosphatidylinositol-4-kinase type IIalpha. *Mol Biol*
896 *Cell* **24**, 2269-2284 (2013).

897 65. C. M. Buckley *et al.*, WASH drives early recycling from macropinosomes and phagosomes to maintain
898 surface phagocytic receptors. *Proc Natl Acad Sci U S A* **113**, E5906-E5915 (2016).

899 66. H. E. Miller, C. L. Larson, R. A. Heinzen, Actin polymerization in the endosomal pathway, but not on
900 the Coxiella-containing vacuole, is essential for pathogen growth. *PLoS Pathog* **14**, e1007005 (2018).

901 67. E. M. Schmid, H. T. McMahon, Integrating molecular and network biology to decode endocytosis.
902 *Nature* **448**, 883-888 (2007).

903 68. W. Kabsch, Xds. *Acta Crystallogr D Biol Crystallogr* **66**, 125-132 (2010).

904 69. P. R. Evans, G. N. Murshudov, How good are my data and what is the resolution? *Acta Crystallogr D*
905 *Biol Crystallogr* **69**, 1204-1214 (2013).

906 70. A. J. McCoy *et al.*, Phaser crystallographic software. *J Appl Crystallogr* **40**, 658-674 (2007).

907 71. P. D. Adams *et al.*, PHENIX: a comprehensive Python-based system for macromolecular structure
908 solution. *Acta Crystallogr D Biol Crystallogr* **66**, 213-221 (2010).

909 72. C. Notredame, D. G. Higgins, J. Heringa, T-Coffee: A novel method for fast and accurate multiple
910 sequence alignment. *J Mol Biol* **302**, 205-217 (2000).

73. H. Ashkenazy *et al.*, ConSurf 2016: an improved methodology to estimate and visualize evolutionary conservation in macromolecules. *Nucleic Acids Res* **44**, W344-350 (2016).

74. J. Jumper *et al.*, Highly accurate protein structure prediction with AlphaFold. *Nature* **596**, 583-589 (2021).

75. M. Mirdita *et al.*, ColabFold: making protein folding accessible to all. *Nat Methods* **19**, 679-682 (2022).

76. M. Mirdita, M. Steinegger, J. Soding, MMseqs2 desktop and local web server app for fast, interactive sequence searches. *Bioinformatics* **35**, 2856-2858 (2019).

77. V. Hornak *et al.*, Comparison of multiple Amber force fields and development of improved protein backbone parameters. *Proteins* **65**, 712-725 (2006).

921 **SUPPLEMENTARY MATERIALS:**

922

923 **Table S1. Thermodynamic parameters for the binding of FAM21 with Retromer by ITC**

924

Syringe	Cell	K_d (nM)	ΔH (kcal/mol)	ΔG (kcal/mol)	$-T\Delta S$ (kcal/mol)
		FAM21 peptides against Retromer			
$FAM21_{R19}$	Retromer	63.5 ± 8.7	-1.2 ± 0.2	-5.7 ± 0.1	-4.5 ± 0.3
$FAM21_{R20}$	Retromer		N.B.		
$FAM21_{R21}$	Retromer	26.8 ± 4.3	-2.8 ± 0.6	-6.2 ± 0.1	-3.4 ± 0.7
		FAM21 peptides against mVps29 – $mVps35_{481-796}$			
$FAM21_{R19}$	mVps29 – $mVps35_{481-796}$	61.1 ± 6.4	-1.9 ± 1.4	-5.8 ± 0.1	-3.8 ± 1.3
$FAM21_{R20}$	mVps29 – $mVps35_{481-796}$		N.B.		
$FAM21_{R21}$	mVps29 – $mVps35_{481-796}$	31.4 ± 1.1	-2.6 ± 1.0	-6.2 ± 0.1	-3.6 ± 1.2
		FAM21 peptides against mVps29			
$FAM21_{R19}$	mVps29		N.B.		
$FAM21_{R20}$	mVps29		N.B.		
$FAM21_{R21}$	mVps29	26.6 ± 2.6	-2.9 ± 0.1	-6.3 ± 0.1	-3.4 ± 0.2

925

926

Table S2. Summary of crystallographic structure determination statistics of Retromer subcomplex with FAM21 repeats.

Data collection statistics	mVPS29 - mVPS35$_{481-796}$ - FAM21$_{R20}$	mVPS29 - mVPS35$_{481-796}$ - FAM21$_{R21}$	mVPS29 - FAM21$_{R21}$
PDB ID	8TTC	8TTA	8TTD
Space group	$P4_32_12$	C121	$P3_221$
Resolution (Å)	46.90 - 3.01 (3.20 - 3.01)	49.31 - 3.46 (3.79 - 3.46)	41.28 - 2.01 (2.06 - 2.01)
a, b, c (Å)	88.76, 88.76, 328.29	123.73, 165.58, 68.00	43.34, 43.34, 165.14
α, β, γ (°)	90.00 90.00 90.00	90.00, 117.51, 90.00	90.00, 90.00, 120.00
Total observations	348,827 (54,935)	110,783 (26,173)	239,643 (17,499)
Unique reflections	27,047 (4,201)	15,793 (3,693)	12,765 (911)
Completeness (%)	99.6 (97.9)	99.3 (97.6)	99.9 (99.0)
R_{merge}[+]	0.137 (1.588)	0.342 (1.233)	0.052 (0.475)
R_{pim}*	0.040 (0.451)	0.139 (0.494)	0.016 (0.152)
CC1/2	0.998 (0.812)	0.993 (0.762)	1.000 (0.972)
$\langle I/\sigma(I)\rangle$	11.7 (1.3)	4.5 (1.3)	25.4 (4.5)
Multiplicity	12.9 (13.1)	7.0 (7.1)	18.8 (19.2)
Molecule/asym	2	2	1
Refinement statistics			
R_{work}/R_{free} (%) ¶[#]	24.90/27.40	22.22/25.39	18.81/24.41
No. protein atoms	7747	7908	1507
Waters	17	10	26
Wilson B (Å^2)	90.59	77.56	42.24
Average B (Å^2)^	101.87	83.95	59.45
Protein	102.13	84.00	59.53
ligands	63.10	85.78	96.35
Water	83.53	41.92	50.70
rmsd bonds (Å)	0.006	0.006	0.007
rmsd angles (°)	1.11	1.08	1.08
Ramachandran plot: Favored/outliers (%)	93.28/1.37	93.42/0.93	94.02/0.54

Values in parentheses refer to the highest resolution shell. [+]$R_{merge} = \Sigma|I - \langle I\rangle| / \Sigma\langle I\rangle$, where I is the intensity of each individual reflection. *R_{pim} indicates all I^+ & I^-. ¶$R_{work} = \Sigma h|F_o - F_c| / \Sigma_l|F_o|$, where F_o *and* F_c are the observed and calculated structure-factor amplitudes for each reflection h. [#]R_{free} was calculated with 10% of the diffraction data selected randomly and excluded from refinement. ^Calculated using Baverage.

935 **Table S3. Thermodynamic parameters for the binding of FAM21 with SNX27 by ITC**

936

Syringe	Cell	K_d (μM)	ΔH (kcal/mol)	ΔG (kcal/mol)	$-T\Delta S$ (kcal/mol)
FAM21 $_{R19-21}$ against SNX27 proteins					
FAM21$_{R19-21}$	hSNX27$_{FL}$	5.70 ± 1.94	-1.51 ± 0.45	-7.18 ± 0.21	-5.67 ± 0.25
FAM21$_{R19-21}$	hSNX27$_{FERM}$	4.97 ± 1.32	-2.50 ± 0.25	-7.25 ± 0.16	-4.75 ± 0.41
FAM21 peptides against hSNX27$_{FL}$					
FAM21$_{R5}$	hSNX27$_{FL}$	23.55 ± 2.19	-1.28 ± 0.15	-6.32 ± 0.05	-5.04 ± 0.10
FAM21$_{R8}$	hSNX27$_{FL}$	68.80 ± 1.27	-2.12 ± 0.04	-5.69 ± 0.01	-3.57 ± 0.05
FAM21$_{R17}$	hSNX27$_{FL}$	70.55 ± 0.64	-2.10 ± 0.57	-5.67 ± 0.01	-3.57 ± 0.58
FAM21$_{R19}$	hSNX27$_{FL}$	6.96 ± 0.12	-2.22 ± 0.17	-7.04 ± 0.01	-4.82 ± 0.18
FAM21$_{R20}$	hSNX27$_{FL}$	19.00 ± 0.28	-1.70 ± 0.28	-6.45 ± 0.01	-4.75 ± 0.29
FAM21$_{R20}$ mutant	hSNX27$_{FL}$	No binding detected			
FAM21$_{R21}$	hSNX27$_{FL}$	No binding detected			
FAM21 peptides against hSNX27$_{FERM}$					
FAM21$_{R5}$	hSNX27$_{FERM}$	29.20 ± 0.28	-3.05 ± 0.62	-6.19 ± 0.01	-3.14 ± 0.61
FAM21$_{R8}$	hSNX27$_{FERM}$	42.50 ± 2.97	-2.87 ± 0.19	-5.97 ± 0.04	-3.11 ± 0.23
FAM21$_{R17}$	hSNX27$_{FERM}$	31.70 ± 0.57	-3.11 ± 0.92	-6.14 ± 0.01	-3.03 ± 0.93
FAM21$_{R19}$	hSNX27$_{FERM}$	38.35 ± 1.34	-3.33 ± 0.52	-6.03 ± 0.02	-2.70 ± 0.49
FAM21$_{R20}$	hSNX27$_{FERM}$	25.55 ± 0.35	-3.00 ± 0.29	-6.27 ± 0.01	-3.27 ± 0.28
FAM21$_{R21}$	hSNX27$_{FERM}$	No binding detected			
FAM21$_{R19}$ peptide against hSNX27$_{FL}$ mutants					
FAM21$_{R19}$	hSNX27$_{FL}$ R437D	No binding detected			
FAM21$_{R19}$	hSNX27$_{FL}$ K495D	58.30 ± 1.41	-2.33 ± 0.34	-5.78 ± 0.01	-3.45 ± 0.35
FAM21$_{R19}$	hSNX27$_{FL}$ K496D	33.53 ± 1.48	-2.97 ± 1.53	-4.99 ± 1.96	-3.14 ± 1.52
FAM21$_{R19}$	hSNX27$_{FL}$ R498D	No binding detected			
FAM21$_{R19}$	hSNX27$_{FL}$ K501D	38.80 ± 0.28	-2.14 ± 0.95	-6.02 ± 0.00	-3.88 ± 0.95

937

938

939

940

Table S4. Summary of crystallographic structure determination statistics for $SNX27_{FERM}$ and FAM21 repeats.

Data collection statistics	$hSNX27_{FERM}$ - $FAM21_{R15}$	$hSNX27_{FERM}$ - $FAM21_{R19}$	$hSNX27_{FERM}$ - $FAM21_{R20}$
PDB ID	8TTT	8TTU	8TTV
Space group	$P2_12_12_1$	$P2_12_12_1$	$P2_12_12_1$
Resolution (Å)	42.95– 2.33	37.54 – 2.36	42.91 – 2.00
	(2.41 – 2.33)	(2.45 – 2.36)	(2.05 – 2.00)
a, b, c (Å)	37.57, 74.37, 105.23 90.00,	37.54, 74.50, 102.53	37.97, 74.20, 105.19
α, β, γ (°)	90.00, 90.00	90.0, 90.0, 90.0	90.0, 90.0, 90.0
Total observations	88510 (5906)	64599 (6238)	139518 (8637)
Unique reflections	12909 (940)	12319 (1195)	20806 (1385)
Completeness (%)	97.6 (75.9)	98.8 (93.5)	99.5 (94.2)
R_{merge}^{+}	0.203 (1.524)	0.097 (0.545)	0.240 (2.161)
R_{pim*}	0.083 (0.632)	0.048 (0.263)	0.101 (0.943)
CC1/2	0.995 (0.379)	0.995 (0.801)	0.989 (0.205)
$\langle I/\sigma(I)\rangle$	7.9 (1.1)	8.4 (1.7)	6.7 (1.0)
Multiplicity	6.9 (6.3)	5.2 (5.2)	6.7 (6.2)
Molecule/asymmetry	1	1	1
Refinement statistics			
R_{work}/R_{free} (%) ¶#	19.05/25.04	20.04/25.26	20.64/26.38
No. protein atoms	2187	2192	2184
Waters	45	28	116
Wilson B ($Å^2$)	39.05	47.82	27.32
Average B ($Å^2$)^	44.23	55.02	36.53
Protein	44.22	54.95	36.51
Ligands	49.37	64.36	39.68
Water	41.71	51.53	36.70
rmsd bonds (Å)	0.009	0.009	0.009
rmsd angles (°)	1.03	0.98	0.98
Ramachandran plot:			
Favored/outliers (%)	95.63/0.79	94.86/1.58	94.80/2.40

Values in parentheses refer to the highest resolution shell. $^{+}R_{merge} = \Sigma|I - \langle I\rangle| / \Sigma\langle I\rangle$, where I is the intensity of each individual reflection. $*R_{pim}$ indicates all I^{+} & I^{-}. $¶R_{work} = \Sigma h|F_o - F_c| / \Sigma_l|F_o|$, where F_o *and* F_c are the observed and calculated structure-factor amplitudes for each reflection h. $^{\#}R_{free}$ was calculated with 10% of the diffraction data selected randomly and excluded from refinement. ^Calculated using Baverage.

950 **Table S5. Key Resources**

951

REAGENT or RESOURCE	SOURCE or REFERENCE	IDENTIFIER
Bacterial Strains		
E. coli BL21 (DE3)	Invitrogen	Catalogue: C600003
Chemicals		
Benzamidine hydrochloride hydrate	Sigma Aldrich	B6506
Deoxyribonuclease I (DNase I)	Sigma Aldrich	DN25
Ampicillin, Sodium Salt	Astral Scientific	A-1414-25g
Kanamycin Sulfate	Astral Scientific	K-1022-25g
Talon® resin	Clontech	635503
Glutathione Sepharose 4B	GE Healthcare	GEHE17-0756-0
Glutathione (reduced form)	Novachem	Catalogue: 077-02016
Isopropyl β-D-1-thiogalactopyranoside	Bioline	Catalogue: BIO-37036
2-Mercaptoethanol (β-ME)	Sigma Aldrich	Catalogue: M6250-100ML
Triton-X100	Sigma Aldrich	X100-500ML
cOmpleteTM EDTA-free protease inhibitor tablet	Sigma Aldrich	Catalogue: 4693159001
EZ-Link Sulfo-NHS-SS Biotin	Thermo Fisher Scientific	Catalogue: 21217
Synthesised peptides		
FAM21-R5$_{536\text{-}552}$ GLFSDEEDSEDLFSSQS	Genscript	N/A
FAM21-R8$_{662\text{-}678}$ TSLFEEDEEDDLFAIAK	Genscript	N/A
FAM21-R15$_{1124\text{-}1140}$ RGEADLFDSGDIFSTGT	Genscript	N/A
FAM21-R17$_{1197\text{-}1213}$ NPFPLLEDEDDLFTDQK	Genscript	N/A
FAM21-R19$_{1261\text{-}1274}$ NLFDDNIDIFADLT	Genscript	N/A
FAM21-R20$_{1289\text{-}1302}$ SIFDDDMDDIFSSG	Genscript	N/A
FAM21-R20$_{1289\text{-}1302\ (IF/SS)}$ S**SS**DDDMDD**SS**SSG	Genscript	N/A
FAM21-R21$_{1328\text{-}1341}$ SNIFDDPLNAFGGQ	Genscript	N/A
Recombinant DNA		
Plasmid: pET-28a human SNX27 $_{FL}$	Gene Universal	N/A
Plasmid: pET-28a human SNX27$_{FERM}$	Gene Universal	N/A
Plasmid: pGEX4T-2 human FAM21$_{R19\text{-}21}$	Gene Universal	
Plasmid: pET-28a human SNX27$_{FL}$ (R437D)	Gene Universal	N/A
Plasmid: pET-28a human SNX27$_{FL}$ (K495D)	Gene Universal	N/A
Plasmid: pET-28a human SNX27$_{FL}$ (K496D)	Gene Universal	N/A
Plasmid: pET-28a human SNX27$_{FL}$ (R498D)	Gene Universal	N/A
Plasmid: pET-28a human SNX27$_{FL}$ (K501D)	Gene Universal	N/A
Plasmid: pEGFP-c1-SNX27 WT and mutants	Simonetti et al 2022	N/A
Plasmid: pEGFP-n1-VPS35 WT and mutants	This study	N/A
Plasmid: pEGFP-c1-Fam21 Tail WT, deletions and mutants	This study	N/A
Plasmid: pXLG3-VPS35-GFP WT and K555N, K556L, K559Q	This study	N/A
Software and Algorithms		
Pymol (version 2.5.4)	Schrodinger, USA.	https://pymol.org/2/

Chimera (version 1.4.0)	Resource for Biocomputing, Visualization, and Informatics, University of California, USA	https://www.cgl.ucsf.edu/chimera/
Prism 7	GraphPad	https://www.graphpad.com/features
Other		
HiLoad® 16/600 Superdex 200 PG	GE Healthcare	Catalogue: 28-9893-35
Mono Q® 10/100 GL	GE Healthcare	Catalogue: 17-5167-01
Amicon™ ultrafiltration devices	Merck	Catalogue: 900000042327 (10K) Catalogue: 900000008078 (30K)
SDS-PAGE BOLT gels	Thermo Fisher Scientific	Catalogue: NW04122BOX (12-well)
NuPAGE 4-12% gels	Thermo Fisher Scientific	Catalogue: NP0336
NuPAGE MOPS SDS running buffer	Thermo Fisher Scientific	Catalogue: NP000102
ChromoTek GFP-Trap Agarose beads	ProteinTech	Catalogue: gta
Streptavidin Sepharose beads	Cytiva	Catalogue: 90100484

952

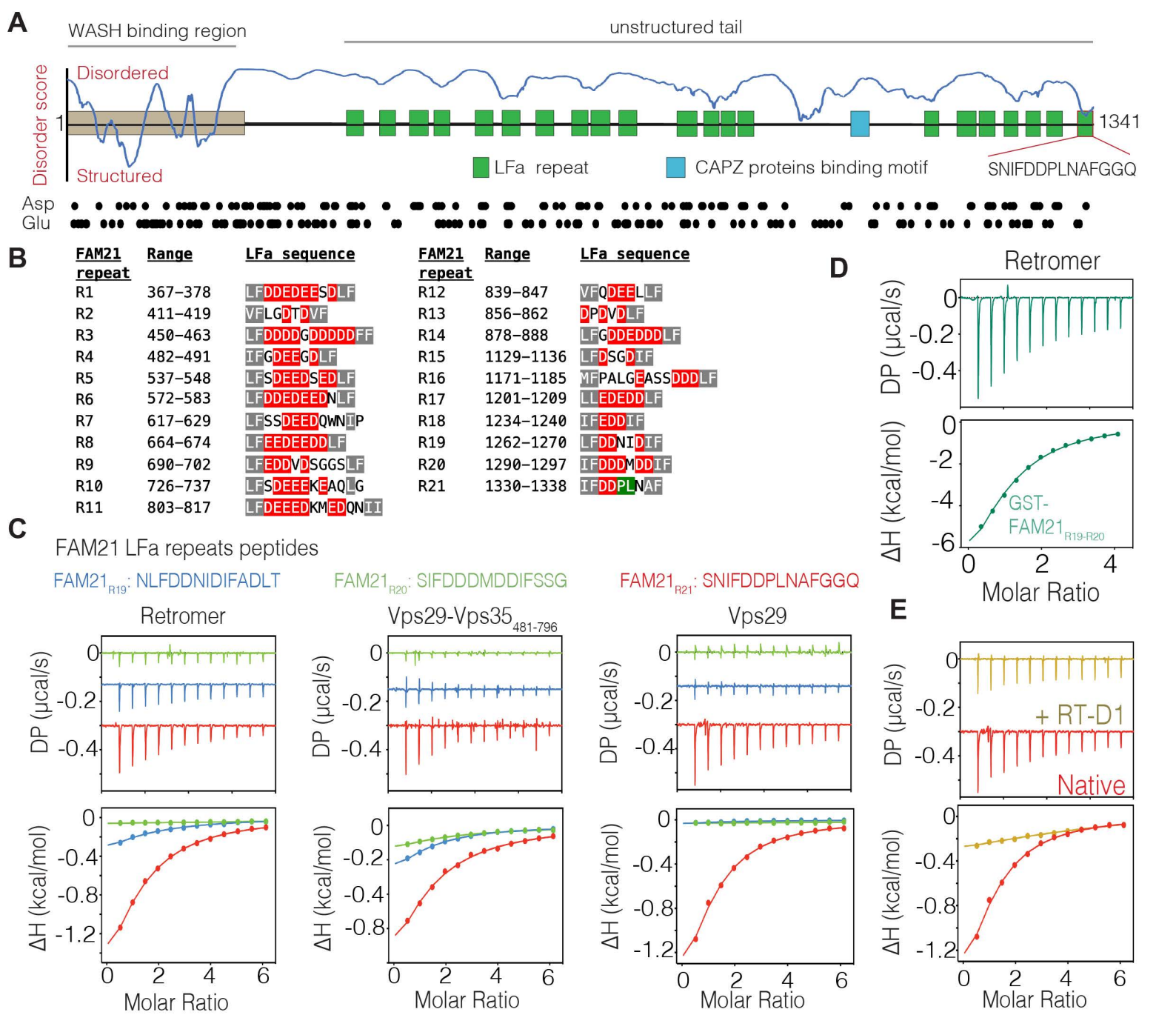

Figure 1. Retromer VPS29 is responsible for binding to repeat 21 of FAM21.
(A) Schematic diagram showing features of human FAM21, and highlighting the 21 LFa repeats in the unstructured tail. (B) Sequences of the 21 LFa repeats within the FAM21 tail. Conserved [I/L]F residues are shown in grey and acidic residues are in red. The PL residues of repeat 21 are highlighted in green. (C) ITC thermograms showing the titration of Retromer, the VPS29–VPS35481-796 subcomplex, and VPS29 alone with FAM21R19 (blue); FAM21R20 (green); and FAM21R21 (red) peptides. (D) Retromer shows binding to GST-FAM21R19-R20. (E) VPS29 and FAM21R21 peptide interaction can be blocked by the addition of the PL-sequence containing cyclic peptide RT-D1. All ITC graphs show the integrated (bottom) and normalized raw data (top) fit with a single-site binding model.

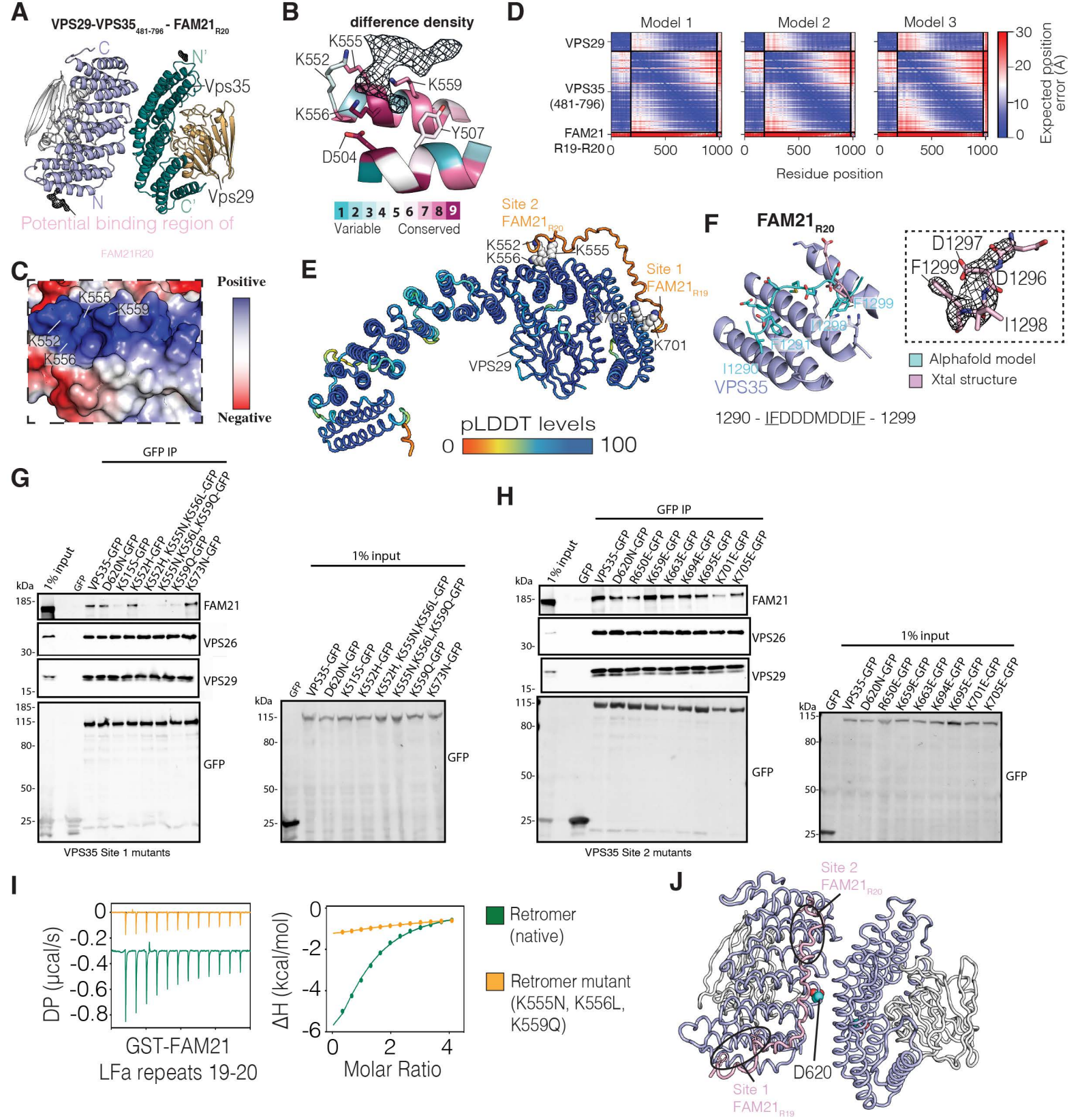

Figure 2. Structural basis for the interaction of LFa repeats with Retromer subunit VPS35.
(A) Overall crystal structure of VPS29–VPS35481-796 in complex with FAM21R20 peptides showing both complexes from the asymmetric unit. (B) VPS35 is highly conserved in the FAM21R20 binding region. The density corresponding to the FAM21R20 peptide is shown in mesh using 2Fo–Fc map contoured at 1σ. Sequence conservation of VPS35 was mapped with CONSURF (Ashkenazy et al., 2016). (C) The electrostatic surface map showing FAM21R20 binding location on VPS35. (D) Predicted alignment Error (PAE) plots of VPS29–VPS35481-796–FAM21R19-R20 complexes generated by Alphafold2. (E) The predicted structure highlighting the per-residue confidence score (pLDDT) between 0 to 100. Regions showing low pLDDT score (green and orange) are likely to be unstructured. (F) Alignment of the Alphafold2 model of FAM21R20 (cyan) and the crystal structure (VPS35 in light purple, FAM21R20 as light pink) highlighting the key interacting residues between FAM21R20 and VPS35. The insert shows the refined electron density of the FAM21R20 peptide observed in the crystal structure. (G) Co-immunoprecipitation (co-IP) of C-terminal GFP-tagged VPS35mutants in the Site 2 binding pocket in HEK293T cells. (H) Co-IP of C-terminal GFP-tagged VPS35 and mutants in the Site 1 binding pocket. Quantitation of these Western blots is shown in Figure S2. (I) ITC analysis showing the binding of GST-FAM21R19-R20 with either native Retromer or VPS35 (K555N/K556L/K559Q) Site 2 mutant. All ITC graphs show the integrated (bottom) and normalized raw data (top) fit with a single-site binding model. (J) The locations of the Site 1 and Site 2 FAM21 repeat binding sites are shown in the context of the VPS35-mediated Retromer dimer assembly derived from cryoelectron tomography (Leneva et al., 2021). The location of the D620N mutation linked to Parkinson's Disease is also indicated in cyan spheres.

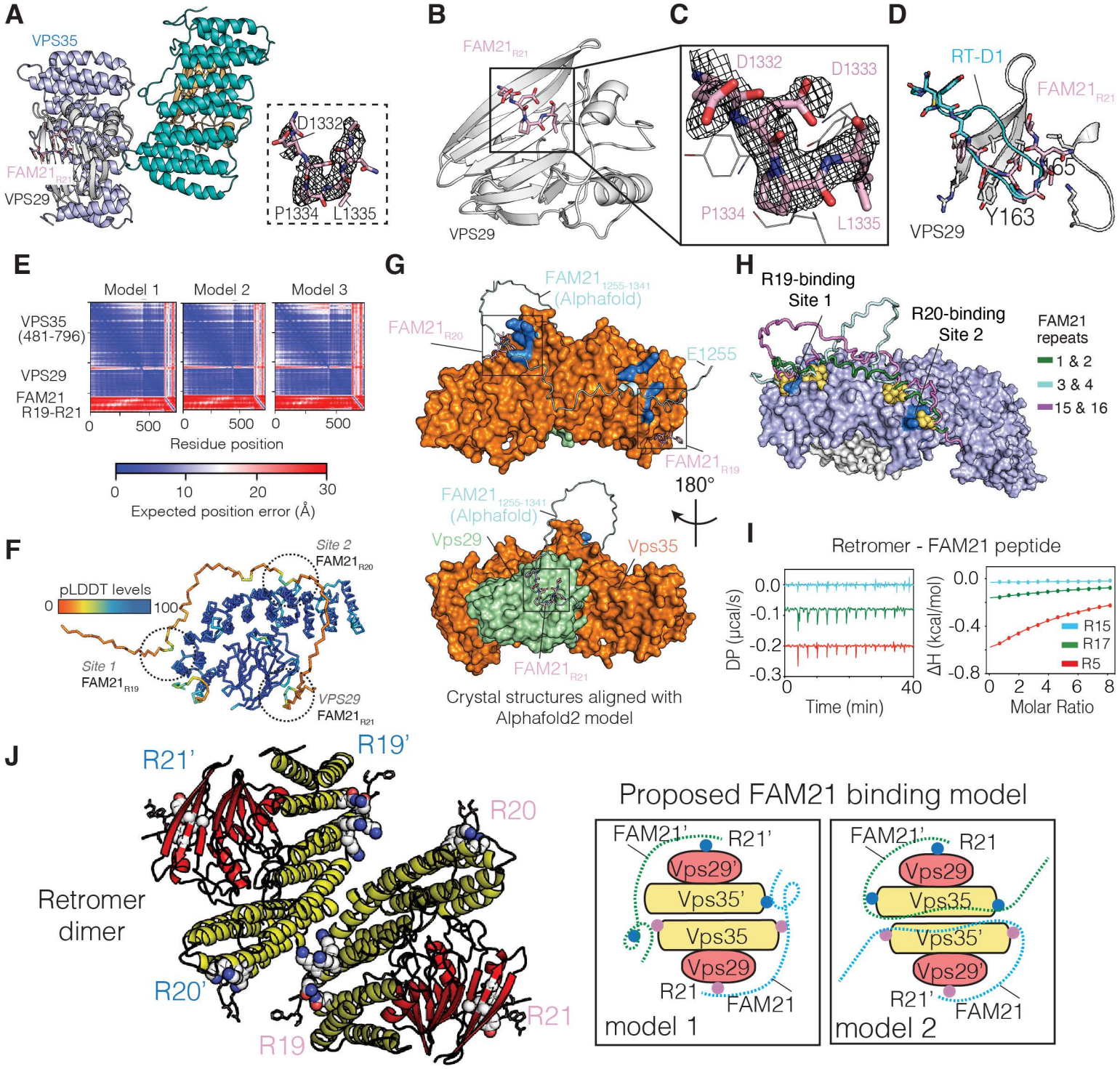

Figure 3. Structural basis for repeat 21 binding to VPS29 and model for Retromer engagement by multiple FAM21 repeats.
(A) Crystal structure of VPS29–VPS35481-796 bound to the FAM21R21 peptide. (B) Crystal structure of VPS29 in complex with FAM21R21 peptide. (C) Enlarged view highlighting the refined density of FAM21R21 peptide peptide (2Fo–Fc map contoured at 1σ). (D) Structural alignment of the VPS29–FAM21R21 peptide complex with the VPS29–RT-D1 cyclic peptide complex (PDB ID 6XS5)(Chen et al., 2021) highlighting the PL motif binding region. (E) Predicted alignment Error (PAE) plots showing the predicted structure of VPS29–VPS35481-796–FAM21R19-R21 complex generated by Alphafold2. (F) The predicted structure highlighting the per-residue confidence score (pLDDT) between 0 to 100. Regions showing low pLDDT score (represents as green and orange) are likely to be unstructured. (G) Superimposition of all the two crystal structures with the Alphafold2 model. (H) Alphafold2 predictions of the complex of VPS29–VPS35 with either FAM21R1-R2, FAM21R3-R4 or FAM21R15-R16 showing pairs of repeats predicted to bind to the same positively charged grooves as repeats FAM2119-20. (I) ITC thermogram showing the binding between Retromer with FAM21R5 (red line), FAM21R15 (blue line) and FAM21R17 (green) peptides. All ITC graphs show the integrated (right) and normalized raw data (left) fit with a single-site binding model. (J) The locations of the FAM21 repeat 19 and 20 binding sites as well as the VPS29-binding repeat 21 are shown in the context of the VPS35-mediated Retromer dimer assembly derived from cryoelectron tomography (Leneva et al., 2021) (PDB ID: 7BLN). The right panel shows two proposed binding models for how FAM21 can bind to a Retromer dimer in cis or trans.

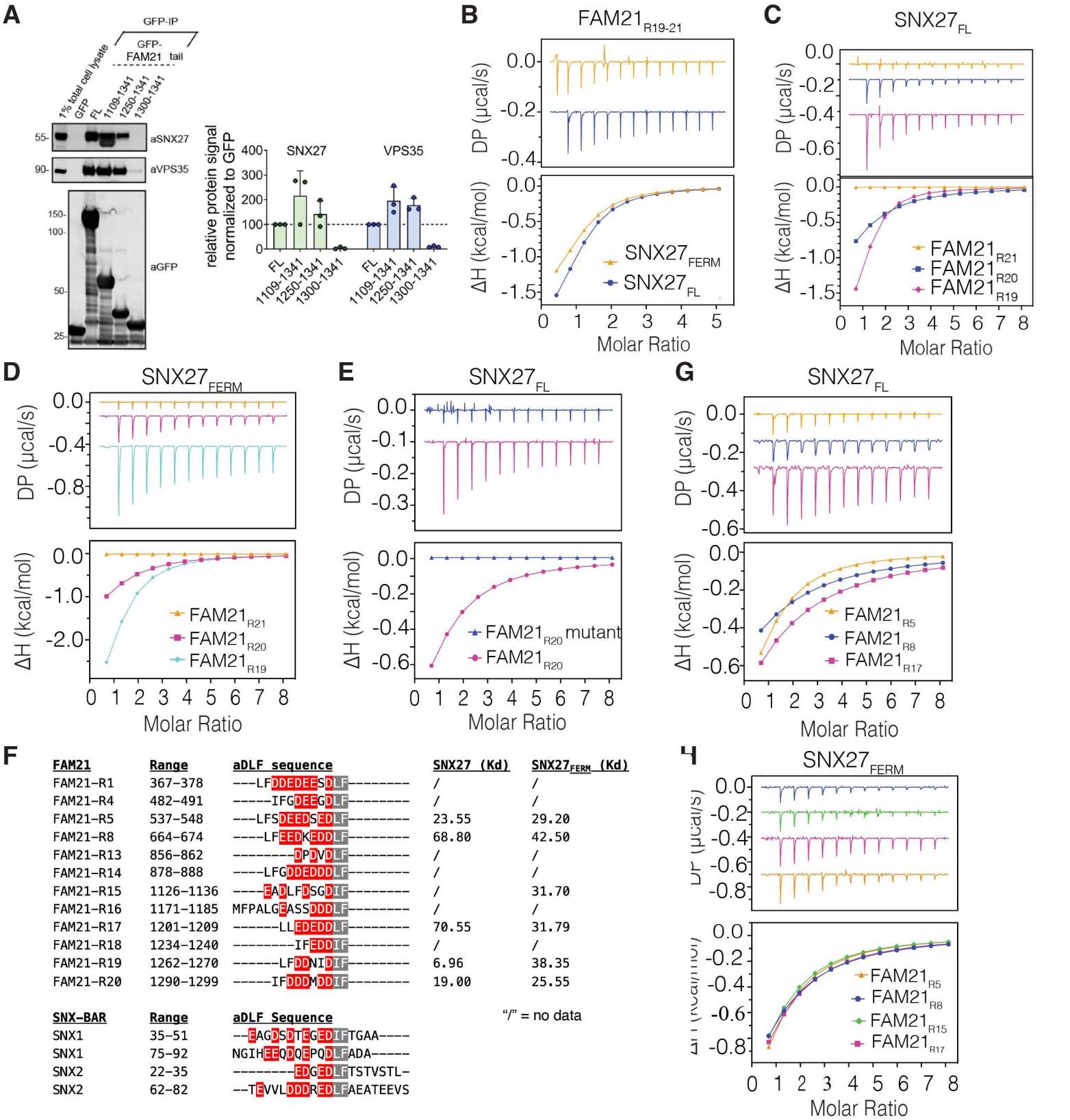

F

FAM21	Range	aDLF sequence	SNX27 (Kd)	SNX27FERM (Kd)
FAM21-R1	367-378	---LFDDEDEESDLF--------	/	/
FAM21-R4	482-491	-----IFGDEEGDLF--------	/	/
FAM21-R5	537-548	---LFSDEEDSEDLF--------	23.55	29.20
FAM21-R8	664-674	----LFEEDKEDDLF--------	68.80	42.50
FAM21-R13	856-862	--------DPDVDLF--------	/	/
FAM21-R14	878-888	----LFGDDEDDDLF--------	/	/
FAM21-R15	1126-1136	----EADLFDSGDIF--------	/	31.70
FAM21-R16	1171-1185	MFPALGEASSDDDLF--------	/	/
FAM21-R17	1201-1209	-------LLEDEDDLF--------	70.55	31.79
FAM21-R18	1234-1240	--------IFEDDIF--------	/	/
FAM21-R19	1262-1270	-------LFDDNIDIF--------	6.96	38.35
FAM21-R20	1290-1299	-----IFDDDMDDIF--------	19.00	25.55

"/" = no data

SNX-BAR	Range	aDLF Sequence
SNX1	35-51	--EAGDSDTEGEDIFTGAA----
SNX1	75-92	NGIHEEQDQEPQDLFADA-----
SNX2	22-35	--------EDGEDLFTSTVSTL-
SNX2	62-82	--TEVVLDDDREDLFAEATEEVS

Figure 4. FAM21 aDLF repeats also binds to the SNX27 FERM domain.
(A) Co-IP of GFP-tagged FAM21 tail in HEK293T cells. Samples were analysed by quantitative fluorescence-based western blotting. The band intensities of SNX27 and VPS35 were measured from n=3 independent experiments using Odyssey software. The SNX27 and VPS35 band intensities, normalized to GFP expression, are presented as the average fraction of the full length FAM21 tail. (B) ITC analysis showing the binding between GST-FAM21R19-21 and SNX27 (yellow line) and SNX27 FERM (blue line). (C) Similar binding experiment showing the binding of FAM21 peptides FAM21R19, FAM21R20 and FAM21R21 with either (C) SNX27 FL or (D) SNX27 FERM. (E) ITC thermogram comparing the binding between native FAM21R20 and 1298IF1299 to SS mutant peptides to SNX27 FL. (F) List of FAM21 peptides containing the same aDLF motif to those observed in SNX1 and SNX2. (G) ITC binding curves of the FAM21R5, FAM21R8 and FAM21R17 peptides titrated into either (G) SNX27 FL or (H) SNX27 FERM. All ITC graphs show the integrated (bottom) and normalized raw data (top) fit with a single-site binding model.

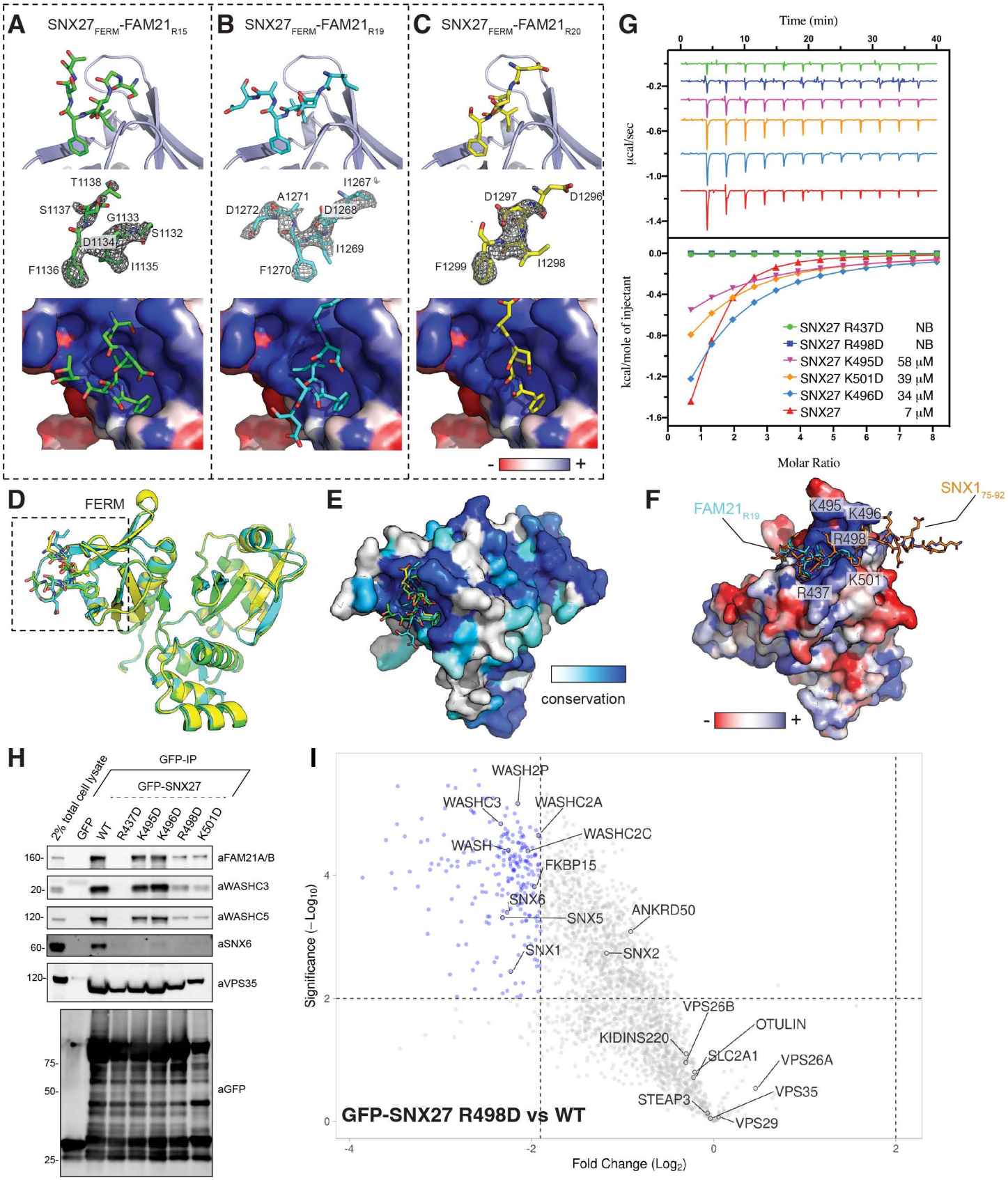

Figure 5. Structural basis for SNX27 interaction with FAM21 aDLF repeats.
(A) Crystal structures of the SNX27 FERM domain bound to aDLF repeats of FAM21. Top views show the key region of SNX27 FERM involved in the binding to the FAM21 aDLF seqeunces (A) FAM21R15, (B) FAM21R19 and (C) FAM21R20. Middle panels show the electron density corresponding to a simulated-annealing composite omit 2Fo–Fc map contoured at 1σ. Bottom panels show electrostatic surface potential of SNX27 highlighting the positively charged pocket of SNX27 FERM. (D) Structural alignment showing the high degree of similarity between all three complex structures. (E) Sequence conservation map highlighting the conserved pocket of SNX27 FERM domain for binding to FAM21 aDLF motifs. (F) Structural alignment of SNX27 bound to FAM21R19 with the SNX27–SNX175-92 complex (PDB ID 7CT1; (Yong et al., 2021)) showing they bind the same pocket. (G) ITC analysis showing the binding of the FAM21R19 peptide with the native or mutant forms of SNX27. The ITC graphs represent the integrated and normalized data fit with 1:1 ratio binding. (H) Co-IP of GFP-SNX27 mutants and binding of WASH, Retromer and ESCPE-1 (represented by SNX6) proteins assessed by Western blot. (I) Proteomic studies comparing the native SNX27 and mutated SNX27 R498D binding capabilities with SNX27 interactors assessed by Co-IP (n = 6; derived from 2 biological repeats each with 3 technical repeats). Mutation of the aDLF binding pocket causes disrupted interactions with most WASH and ESCPE-1 subunits. The full list of detected proteins is provided in Dataset S1.

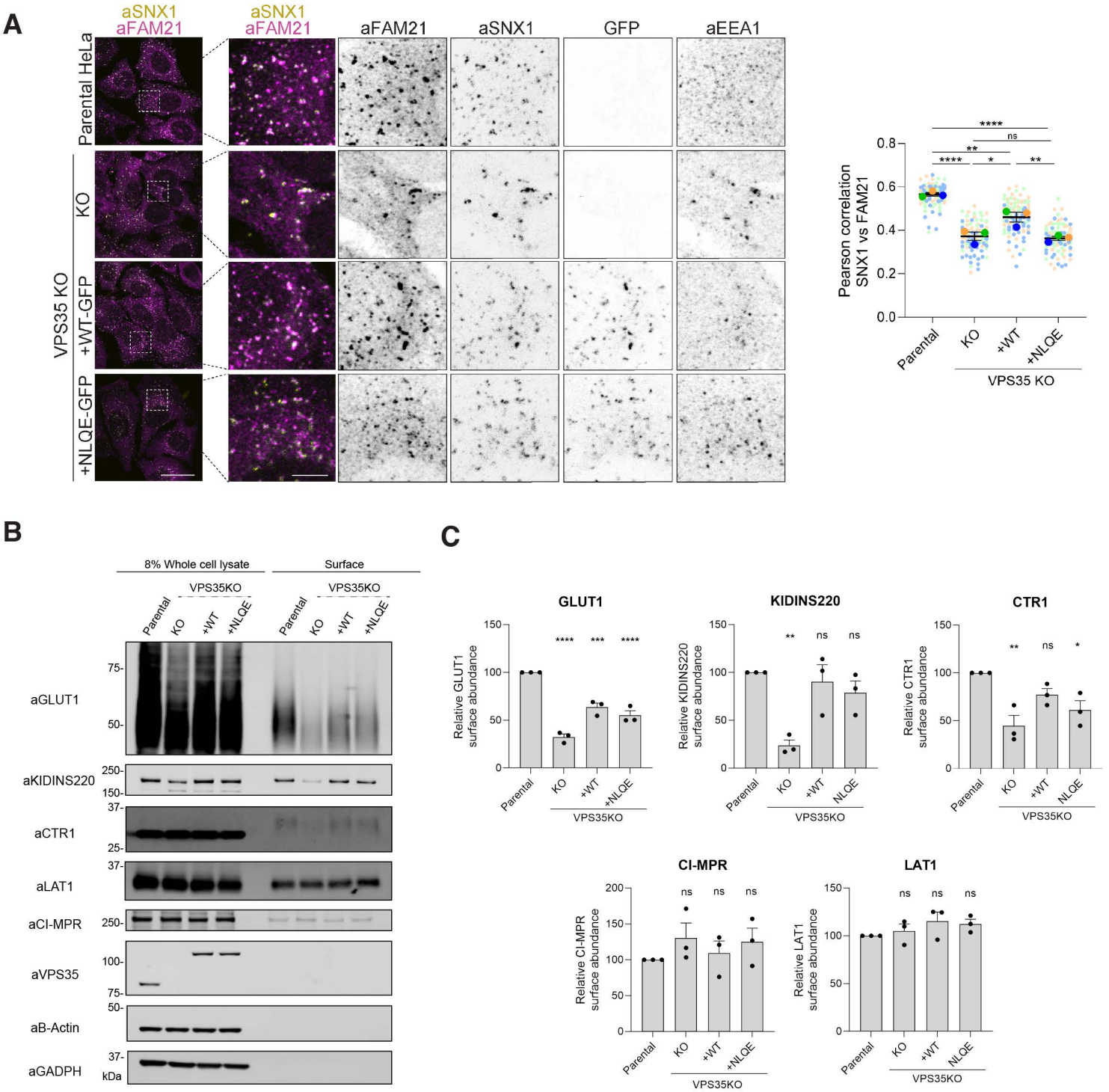

Figure 6. VPS35 interaction with FAM21 contributes to its endosomal localization, but it is not strictly required for SNX27–Retromer recycling. (A) VPS35 KO HeLa cells show a reduction in the colocalisation of FAM21 to SNX1-positive endosomal domains. Re-expression of VPS35-GFP WT can partially rescue this mislocalistion, but the mutant VPS35(NLQE)-GFP with both FAM21 sites mutated is unable to restore FAM21 recruitment levels. A total of 90 cells were analyzed in each condition for colocalization between SNX1 and FAM21 across n=3 independent experiments. (B) VPS35 KO HeLa cells showed reduced cell surface levels of SNX27–Retromer dependent cargos including GLUT1 and KIDINS220. VPS35 KO clonal line was stably transduced with lentiviral particles containing VPS35-GFP WT or VPS35(NLQE)-GFP. Re-expression and rescue with both constructs is able to rescue the cell surface levels of these cargos. This indicates that full binding of FAM21 to VPS35 is not strictly required for SNX27–Retromer mediated endosomal recycling. (C) Quantitation of Western blots is shown. Similar results were obtained in H4 cell lines as shown in Figure S5C. Statistics for western blots and confocal microscopy images were calculated from a minimum of 3 independent experimental repeats Graphs were plotted representing the mean value ± the standard error (SE) for each experimental condition. s. In all graphs, * = $p < 0.05$, ** = $p < 0.01$, *** = $p < 0.001$, **** = $p < 0.0001$.

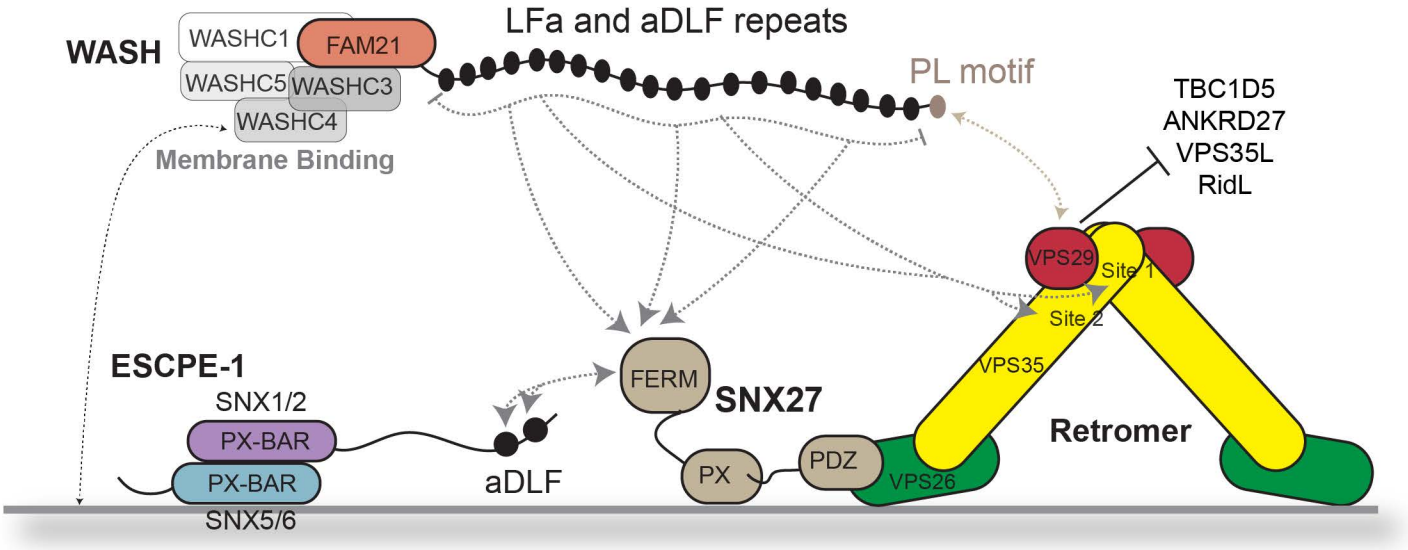

Figure 7. Summary and proposed model for the cooperative recruitment of FAM21 by Retromer, SNX27 and other endosomal proteins. The WASH subunit FAM21 has 21 LFa repeated elements in its extended tail that are rich in acidic, isoleucine and phenylalanine residues. LFa sequences possess two [L/I]F motifs interspersed by an acidic stretch ([L/I]F[D/E]3-9[L/I]F). These bind two conserved sites towards the C-terminus of the VPS35 subunit of Retromer. The last repeated element of FAM21 has a specific PL dipeptide sequence that promotes interaction with Retromer subunit VPS29. This would be mutually exclusive of binding to other VPS29 interactors such as TBC1D5, ANKRD27, VPS35L and bacterial effector RidL. aDLF sequences are a subset of the LFa repeats with an acidic stretch prior to a D[L/I]F motif that associate with a conserved pocket in the SNX27 FERM domain, and are also found in the SNX1 and SNX2 proteins of the ESCPE-1 complex.

```
                                                                                                                                                                                                                                                                                                                                                                                                                                                                                                                                                                                                                                                                                                                                                                                                                                                                                                                                                                                                                                                                                                                                                                                                                                                                                                                                                                                                                                                                                                                                                                                                                                                                                                                                                                                                                                                                                                                                                                                                                                                                                                                                                                                                                                                                                                                                                                                                                                                                                                                                                                                                                                                                                                                                                                                                                                                                                                                                                                                                                                                                                                                                                                                                                                                                                                                                                                                                                                                                                                                                                                                                                                                                                                                                                                                                                                                                                                                                                                                                                                                                                                                                                                                                                                                                                                                                                                                                                                                                                                                                                                                                                                                                                                                                                                                                                                                                                                                                                                                                                                                                                                                                                                                                                                                                                                                                                                                                                                                                                                                                                                                                                                                                                                                                                                                                                                                                                                                                                                                                                                                                                                                                                                                                                                                                                                                                                                                                
hFam21     1  SNLFDDNIDIFADLT..VKPKEK.SKKKV.EAKSIFD..DDMDDIFSSG.....IQAK
mFam21     1  PNLFDDNIDIFADLT..VKPKEK.SKKKV.AAKSMFD..DDTDDIFSSG.....LQAK
rFam21     1  PNLFDDNIDIFADLT..VKPKEK.PKKKV.TAKSMFD..DDTDDIFSSG.....LQAK
bFam21     1  SNLFDDNIDIFADLT..VKPKEK.SKKKV.EAKSIFD..DDTDDIFSSG.....IQTK
dFam21     1  TSLFSSD.DEEAEVP..VKSAPA.KKLPVKPSKSLFSDDDDDDDLFGGSSTSKAAAK
zfFam21    1  ASLFDDDVDIFADLTGTSKPKEKKAKKKV.ETKSIFD..DDMDDIFSTG.....TTKP
```

Repeat 19 Repeat 20

```
                                                                                                                                                                                                                                                                                                                                                                                                                                                
hFam21    48  TTKPKSRSAQA..APEPRF.EHK....VSNIFDDPLNAFGG.Q
mFam21    48  ASKPKSQSAEA..ASEQRS.EHK....VASIFDDPLNAFGS.Q
rFam21    48  ASKPKSQSAEA..VSELRS.ENK....VSNIFDDPLNAFGS.Q
bFam21    48  TTKSKSRSSQK..VTESRS.GQK....VSNIFDDPLNAFGG.Q
dFam21    55  KTKPAARTASK..PPASKT.TTPTATIPSNSGDNPLADLLDFK
zfFam21   51  TVKPSSKSKKSQPIQEPASTAET....AHNIFDDPLNAFGG.N
```

Repeat 21

Figure S1. Sequence alignment of FAM21/WASHC2 repeats 19, 20 and 21.
Repeats 19-21 of FAM21 are aligned from various species. Conserved [I/L]F dipeptide motifs are indicated by yellow arrows while the specific PL motif in repeat 21 is indivated by green ovals. h, homo sapiens; m, Mus musculus; r, Rattus norvegicus; b, Bos taurus; d, Drosophila melanogaster; zf, Danio rerio.

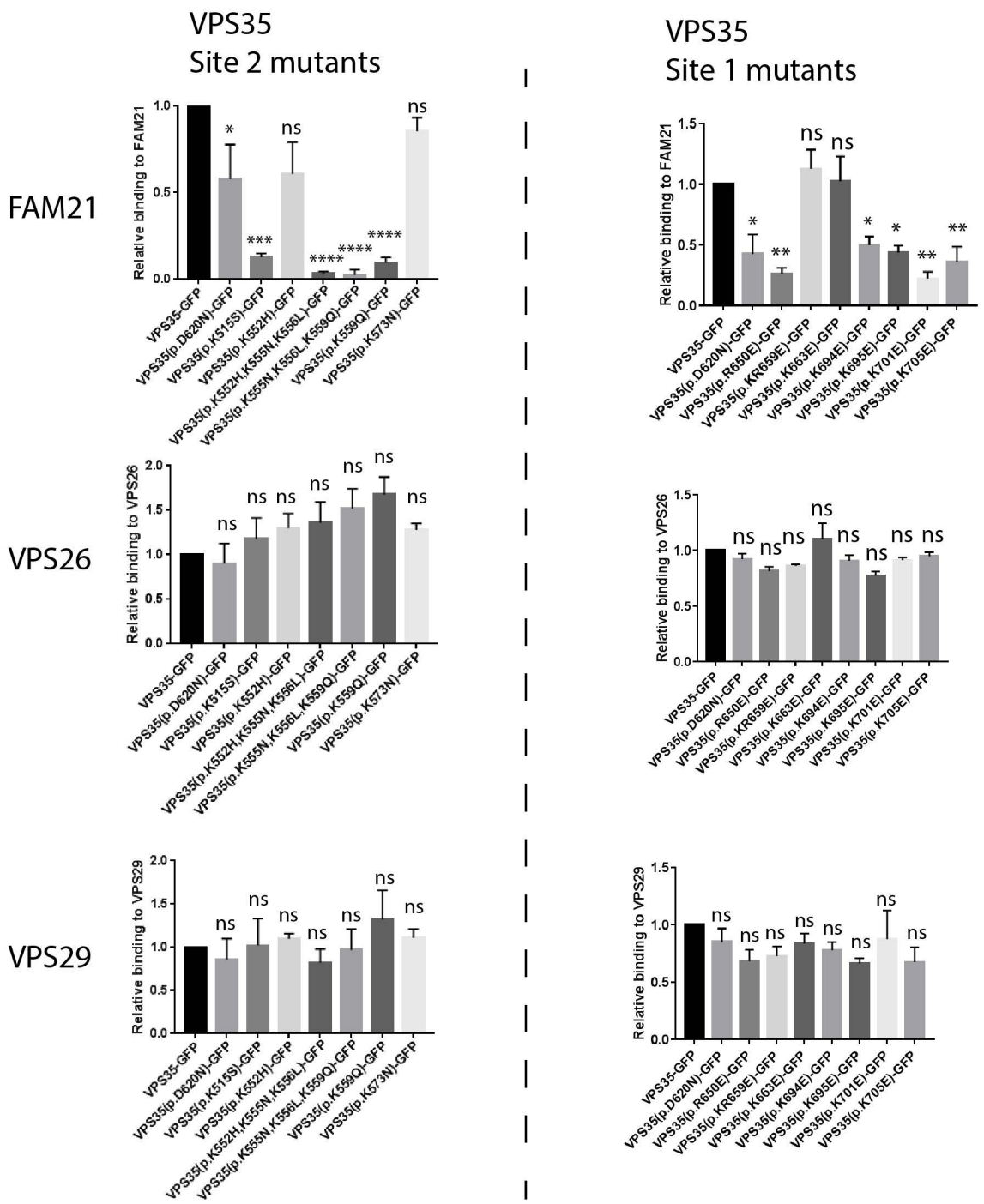

Figure S2. Quantitation of the Western blots shown in Figure 2G and 2H.
Band intensities from Figure 2G and 2H were quantified using Odyssey software and normalized to GFP expression. 1-way ANOVA with Dunnett's multiple comparisons test. Error bars represent the standard error. *P < 0.05, **P < 0.01, ***P < 0.001, ****P < 0.0001.

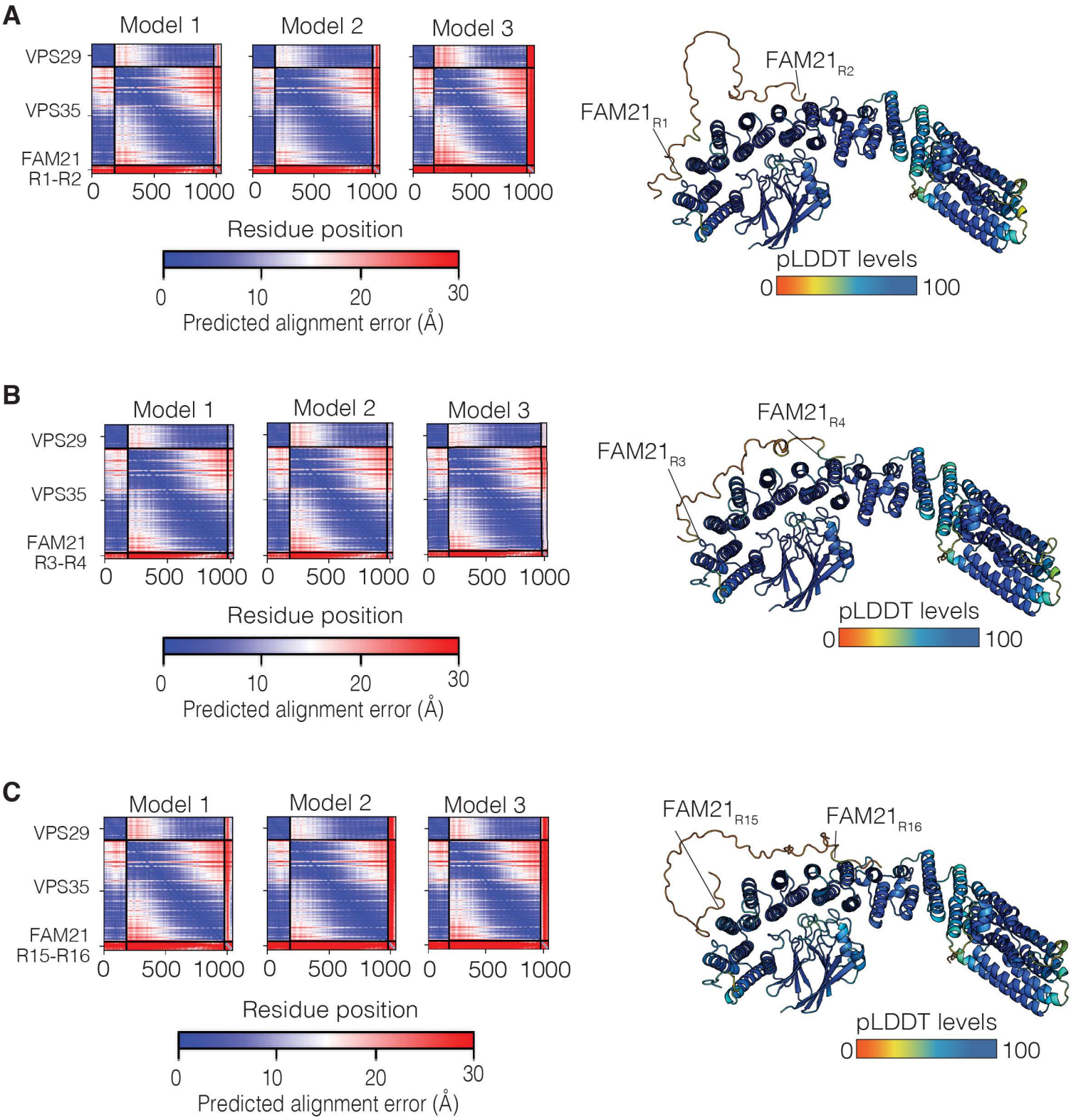

Figure S3. Alphafold models of VPS35–VPS29 in complex with different FAM21 LFa repeats.
(A) Predicted alignment Error (PAE) plots for the AlphaFold2-predicted structures of the human (A) VPS35–VPS29–FAM21R1-R2 complex, (B) VPS35–VPS29–FAM21R3-R4 complex, (C) VPS35–VPS29–FAM21R15-R16 complex. On the right the predicted structures are shown coloured according to the per-residue confidence score (pLDDT) between 0 to 100. Regions showing a low pLDDT score (green and orange) are likely to be unstructured.

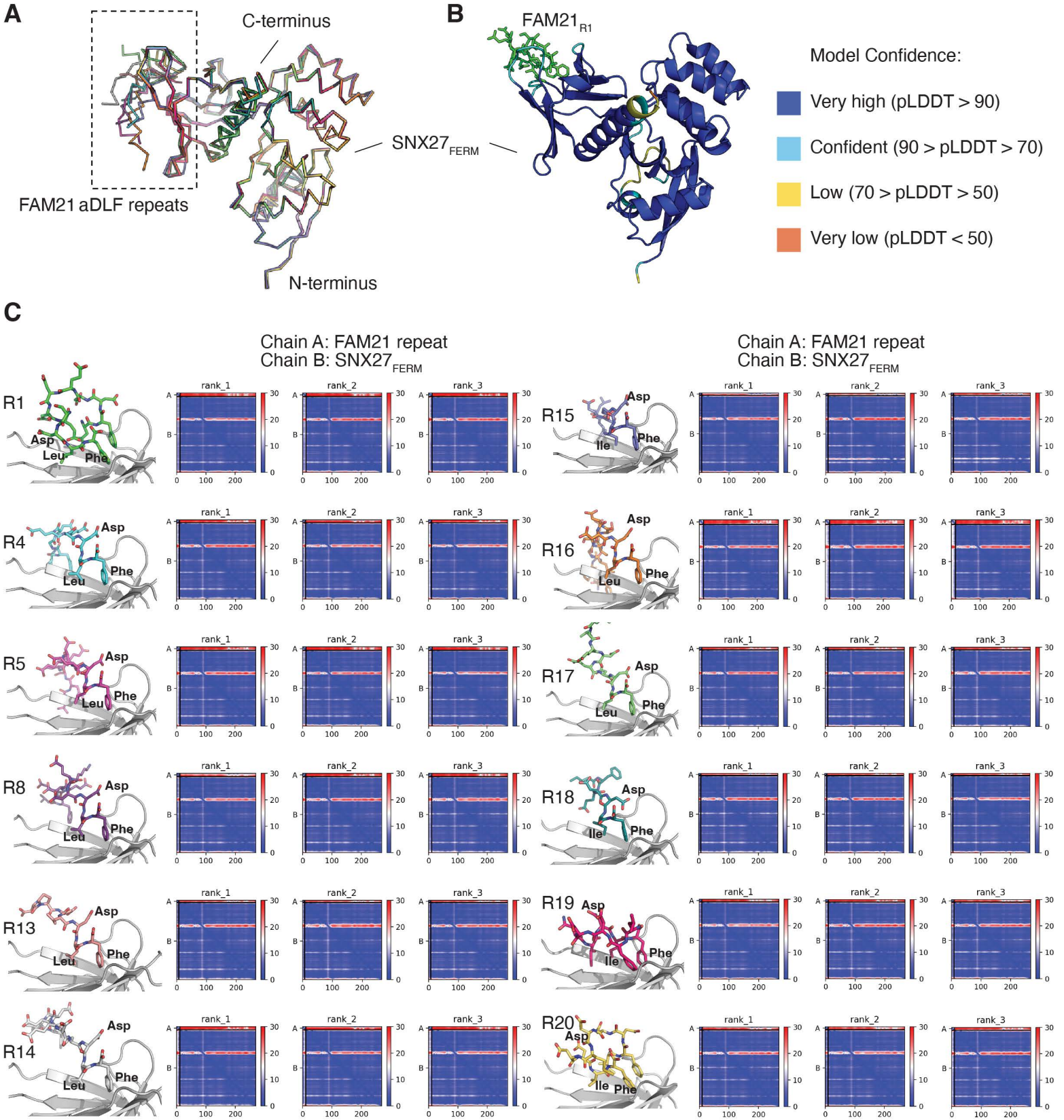

Figure S4. Alphafold models of SNX27 FERM domain in complex with various FAM21 aDLF sequences.
(A) Overlay of all AlphaFold2 predicted structures shown as Cα backbone ribbon. The sequences of the aDLF repeats are shown in Figure 4F. (B) The predicted complex of SNX27FERM bound to FAM21 aDLF sequence from repeat 1. SNX27 is shown in cartoon representation coloured according to pLDDT score. The FAM21R1 peptide is shown in green sticks. (C) Predicted alignment Error (PAE) plots showing the predicted structure of human SNX27FERM–FAM21 aDLF complexes. The top ranked prediction is shown in close up in the left hand panels.

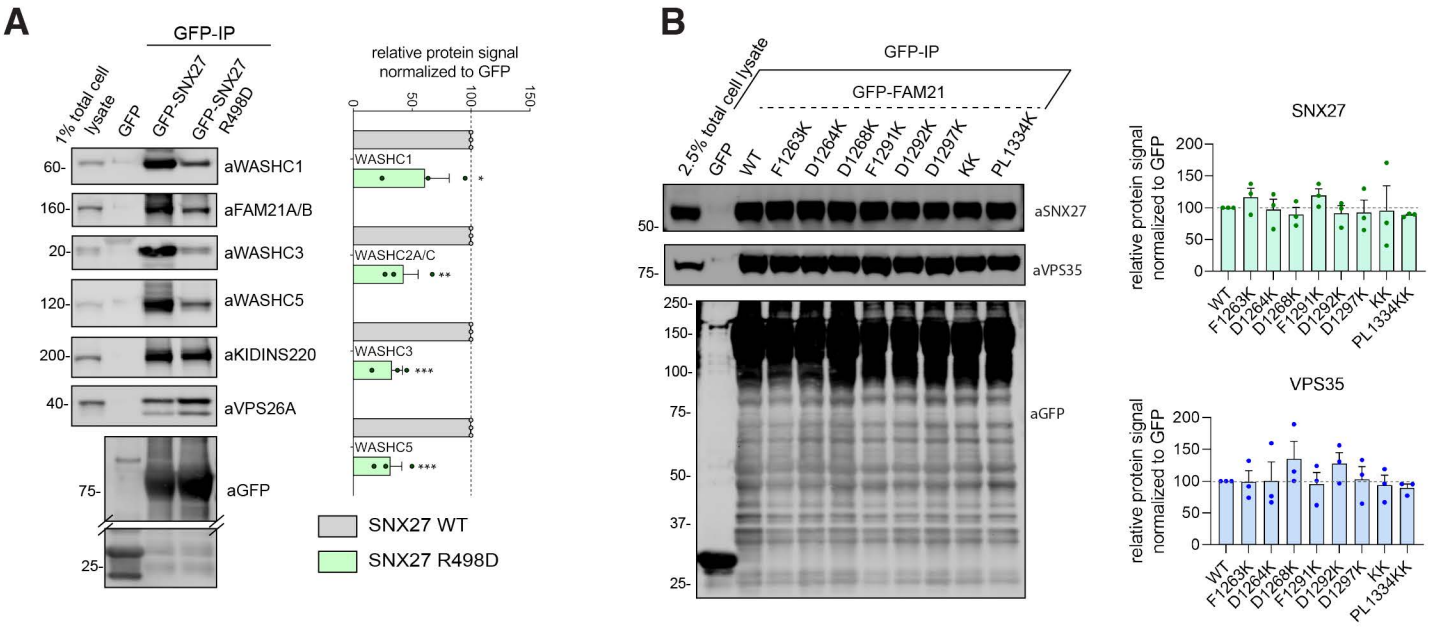
A
GFP-IP
1% total cell lysate
GFP
GFP-SNX27
GFP-SNX27 R498D
60-
160-
20-
120-
200-
40-
75-
25-
aWASHC1
aFAM21A/B
aWASHC3
aWASHC5
aKIDINS220
aVPS26A
aGFP
relative protein signal normalized to GFP
0
50
100
150
WASHC1
WASHC2A/C
WASHC3
WASHC5
SNX27 WT
SNX27 R498D
B
GFP-IP
GFP-FAM21
2.5% total cell lysate
GFP
WT
F1263K
D1264K
D1268K
F1291K
D1292K
D1297K
KK
PL1334K
aSNX27
aVPS35
aGFP
SNX27
VPS35
relative protein signal normalized to GFP

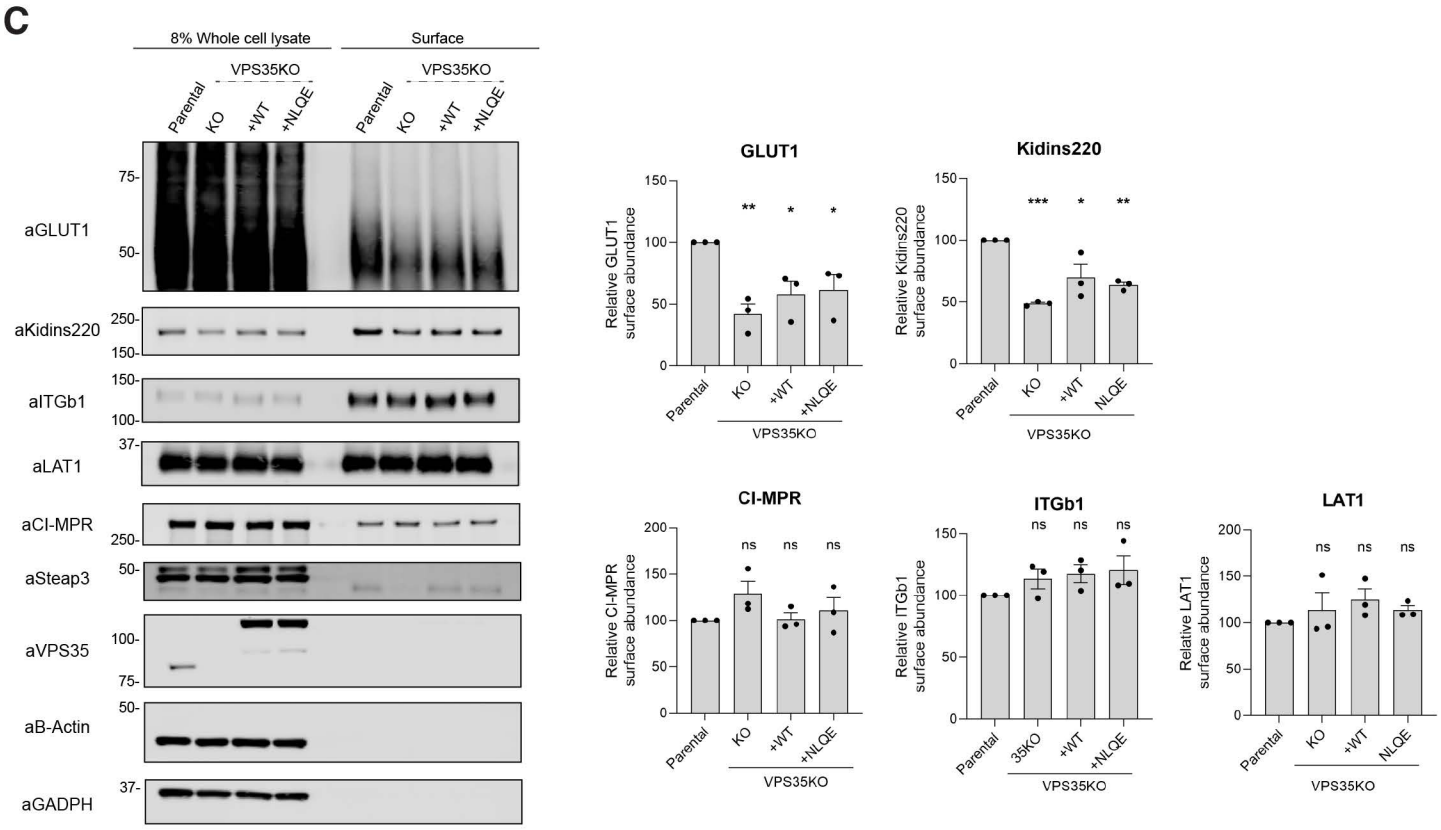
C
8% Whole cell lysate
Surface
VPS35KO
Parental
KO
+WT
+NLQE
aGLUT1
aKidins220
aITGb1
aLAT1
aCI-MPR
aSteap3
aVPS35
aB-Actin
aGADPH
GLUT1
Kidins220
CI-MPR
ITGb1
LAT1
Relative GLUT1 surface abundance
Relative Kidins220 surface abundance
Relative CI-MPR surface abundance
Relative ITGb1 surface abundance
Relative LAT1 surface abundance
ns